Application of the complex differentiation method to the sensitivity analysis of aerodynamic noise

Hugo Vincent, Christophe Bogey

Application of the complex differentiation method to the sensitivity analysis of aerodynamic noise

Hugo Vincent, Christophe Bogey,

[a] *Univ Lyon, Ecole Centrale de Lyon, CNRS, Univ Claude Bernard Lyon 1, INSA Lyon, LMFA, UMR5509, 69130, Ecully, France*

Abstract

The complex differentiation method (CDM) is applied to the sensitivity analysis of the noise generated by two-dimensional mixing layers, simulated by Direct Numerical Simulation (DNS), in order to investigate its capabilities to highlight the effects of a key parameter on the aerodynamic noise. For this purpose, simulations are carried out using the CDM for different flow Mach numbers, Reynolds numbers and mesh spacings. In each case, the derivatives of the noise levels with respect to one of the three parameters are obtained using the CDM, implemented by adding a small imaginary perturbation to the parameter under study. In most cases, vortex pairings occur in the mixing layers and produce acoustic waves at a single frequency. The derivatives of the acoustic intensity obtained using the CDM show that the sound radiation is stronger and less directed downstream as the Mach number increases, in agreement with dimensional analyses. They also indicate that the radiation is more intense and directive as the Reynolds number increases. The magnitude of the derivatives of the acoustic intensity with respect to the mesh size decreases for finer meshes, showing that the grid sensitivity of the radiated noise is reduced for the latter meshes, as expected. In all cases, the derivatives obtained using the CDM are in good agreement with results from parametric studies. This suggests that the CDM can be used to describe the effects of physical parameters and of the grid resolution on the sound produced by a high-speed flow.

Keywords: complex differentiation method, sensitivity analysis, grid sensitivity, mixing layer, direct numerical simulation, aeroacoustics

1. Introduction

Reducing the noise produced by flows is required in many industrial applications. To develop suitable strategies for that, it is often necessary to highlight the effects of flow parameters such as the Mach and Reynolds numbers on the noise generation mechanisms. Parametric studies are often conducted using high-fidelity simulations to bring these effects to light. For instance, to examine the effects of the Mach number on the noise produced by a jet, several simulations of the jet at different Mach numbers should be analyzed. For a high-Reynolds number flow, a huge number of mesh points are required to accurately resolve the aerodynamic and acoustic fields, leading to parametric studies of prohibitive cost.

A sensitivity analysis can be seen as an alternative. It enables to estimate the derivatives of the flow solutions with respect to a parameter, namely, the flow sensitivities. For example, the derivative of a function f (e.g., noise

Email address: hugo.vincent@ec-lyon.fr (Hugo Vincent)

level) with respect to a parameter α, at a point $\alpha = \alpha_0$, can be written as

$$\frac{\mathrm{d}f}{\mathrm{d}\alpha}(\alpha_0) = \lim_{\epsilon \to 0} \frac{f(\alpha_0 + \epsilon) - f(\alpha_0)}{\epsilon} \ , \tag{1}$$

where ϵ is a real number. A high value of the derivative indicates a strong sensitivity of the function f to a variation of the parameter α at $\alpha = \alpha_0$. Conversely, a low value of the derivative means that the function is only slightly affected by the parameter variation.

Various sensitivity analysis methods are available in the literature, as documented in the review by Martins & Hwang [1]. The most notable ones are methods based on Taylor approximations [2], the sensitivity equation method [2, 3, 4, 5, 6] and the complex differentiation method [2, 7, 8, 9], also called the complex-step method. With a method based on Taylor approximations, values of the derivatives of the flow solutions with respect to a parameter are estimated by carrying out several simulations. For instance, a first-order approximation of the derivative of a function f can be written as

$$\frac{\mathrm{d}f}{\mathrm{d}\alpha}(\alpha_0) \simeq \frac{f(\alpha_0 + h) - f(\alpha_0)}{h} \ , \tag{2}$$

where h is a real number denoting a perturbation magnitude. To estimate the derivative using this approximation, it is necessary to carry out a simulation for $\alpha = \alpha_0 + h$ and another one for $\alpha = \alpha_0$. The truncation error of a Taylor approximation is reduced as the perturbation magnitude h decreases. Therefore, it is recommended to consider very small values for h. However, when h is excessively small, $f(\alpha_0 + h)$ and $f(\alpha_0)$ are so close that their difference is lower than the rounding errors and thus the derivative $\mathrm{d}f/\mathrm{d}\alpha$ increases as h becomes smaller, as shown by Anderson *et al.* [8] and Martins *et al.* [10], among others. Finding a value of the perturbation magnitude h to accurately evaluate the derivatives of interest therefore may require several trials.

Flow sensitivities can also be estimated using the sensitivity equation method (SEM). This method consists in solving the sensitivity equations obtained by differentiating the Navier-Stokes equations with respect to a parameter. The solutions of these equations are the derivatives of the flow variables with respect to the parameter and can thus be used to determine the flow sensitivities. The flow variables are involved in the sensitivity equations due to the non-linearity of the Navier-Stokes equations. To apply the SEM, it is thus required to solve the sensitivity equations in conjunction with the Navier-Stokes equations to compute the flow variables and the flow sensitivities. SEM has been used several times to study unsteady incompressible flows. For instance, Hristova *et al.* [5] investigated the sensitivity of a two-dimensional pulsed flow around a square cylinder with respect to the mean flow velocity, the amplitude and the period of the pulsation using SEM. Their results showed that the asymmetrical vortex shedding downstream of the cylinder appears more clearly and earlier in the flow sensitivity fields than in the flow solution fields. The SEM was first applied to a three-dimensional turbulent flow by Kirkman & Metzger [11] to describe the effects of the Reynolds number on a channel flow. The variations of the mean flow fields with the Reynolds number, predicted by the flow sensitivities obtained by the authors, were in good agreement with the results of parametric studies. Zayernouri & Metzger [6] studied the effects of the Reynolds and Prandtl numbers on vortices in a non-isothermal two-dimensional mixing layer using the SEM. The vorticity fields and their derivatives with respect to these numbers estimated by the authors indicated that the vortices are more isolated from each other as the Reynolds number increases and that the temperature is less homogeneous within the vortices when the Prandtl number is higher.

Finally, the complex differentiation method (CDM) can be used to obtain the flow sensitivities. It is related to the Taylor approximations. However, it allows to determine the derivatives of the flow solutions with respect to a parameter by performing a single simulation, and without round-off errors [12]. It consists in adding a small imaginary perturbation to the parameter and solving the Navier-Stokes equations using complex arithmetic. It can be implemented in a simple way in a computational code dealing only with real variables [8, 10, 13]. The complex differentiation method was introduced by Lyness & Moler [7], and then been applied by Squire & Trapp [12] to evaluate the derivatives of analytical real functions. It was later used by Anderson *et al.* [8] and Vatsa [13] for turbulent flows by solving the time-dependent Reynolds-averaged Navier-Stokes equations, and by Cerviño *et al.* [14] and Lu & Sagaut [9] for two-dimensional compressible unsteady flows using DNS. The method was then used by Vergnault & Sagaut [15] in conjunction with the Lattice Boltzmann Method to analyze the sensitivity of a flow around a cylinder with respect to the Reynolds number. Subsequently, the CDM was coupled with a time-reversal technique to localize noise sources within a two-dimensional mixing layer [16]. Finally, Kirkman & Metzger [2] studied the sensitivity of a channel flow to the channel height, the viscosity and the pressure gradient using second-order Taylor approximations, the SEM and CDM. The results obtained by these authors indicate that among these three approaches, the CDM is the most accurate and the cheapest in terms of numerical cost.

Given the preceding, CDM appears to be a straightforward and accurate method for performing sensitivity analyses. However, it is still unclear if it can be used to study the effects of physical parameters on the noise produced by a flow. Another question is whether a sensitivity analysis can help to characterize the accuracy of acoustic variables computed by direct numerical simulations. A grid sensitivity study is the standard method to assess this accuracy. It consists in carrying out simulations using finer and finer meshes. The convergence of the flow solutions with mesh refinement is then chosen as a criterion for numerical accuracy [17]. The derivatives of the flow solutions with respect to the mesh spacing may provide useful information to study this convergence, since they indicate how the flow solutions vary with a small change in the grid resolution. To the best of the authors' knowledge, the CDM has not been applied yet to conduct a grid sensitivity analysis of the aerodynamic and acoustic fields of a high-speed flow computed by direct numerical simulation.

To answer the above questions, CDM is applied in this work to study the effects of the Mach number, the Reynolds number, and the mesh spacing on the noise produced by a two-dimensional subsonic mixing layer. The mixing layer is controlled with a harmonic excitation so that vortex pairings occur and produce acoustic waves at a single frequency, as in other studies in the literature [16, 18, 19]. Parametric studies are conducted by carrying out direct numerical simulations of the mixing layer for different Mach and Reynolds numbers, based on the velocity difference between the fast and the slow flows of the mixing layer and on the inlet vorticity thickness δ_ω, and using several meshes. The values of the Mach number are between 0.2 and 0.4 and those of the Reynolds number are between 400 and 12800. Four non-uniform structured grids, differing from each other by the mesh spacing at the center of the mixing layer, denoted Δy_0, which varies from $0.1\delta_\omega$ to $0.8\delta_\omega$, are considered. In each simulation, the complex differentiation method is used to estimate the derivatives of acoustic variables with respect to the Mach number, the Reynolds number or the mesh spacing parameter Δy_0. In this way, comparisons between the flow sensitivities obtained using the CDM and the results of the parametric studies can be made.

The paper is organized as follows. The compressible Navier-Stokes equations, the complex differentiation

method, the complex Navier-Stokes equations and the sensivity equations are presented in Section 2. In Section 3, the parameters of the mixing layer and the numerical parameters of the simulations are given. In Section 4, the accuracy of the complex differentiation method is compared with that of a first-order approximation by estimating the derivative of the acoustic power of mixing layers at different Reynolds numbers with respect to the latter parameter. The approach employed to estimate the flow sensitivities with respect to the Reynolds and Mach numbers, and to the mesh spacing Δy_0 using the complex differentiation method is described in Section 5. The results are given in Section 6. The effects of the Mach number on the sound radiation of the mixing layer are first described by analyzing the properties of acoustic fields, such as the root-mean-square values of pressure fluctuations. They are then compared to the derivatives of the sound intensities with respect to the Mach number estimated using the CDM. To investigate the efficiency of the CDM, the derivatives of the noise levels provided by the flow sensitivities are compared with the noise levels values. The results obtained from the simulations performed with different Reynolds number and grids are analyzed with the same approach.

2. Governing equations and complex differentiation method

2.1. Navier-Stokes equations

The compressible Navier-Stokes equations in their conservative form are considered. They describe the evolution of density ρ, momentum $\mathbf{m} = \rho\mathbf{u}$, where $\mathbf{u}$ is the velocity vector, and total energy $E = p/(\gamma - 1) + (\mathbf{m} \cdot \mathbf{m})/2\rho$, where p is the pressure, γ is the adiabatic index, and the interpunct denotes the scalar product. They can be written as follows

$$\frac{\partial \rho}{\partial t} + \nabla \cdot \mathbf{m} = 0 \,, \tag{3}$$

$$\frac{\partial \mathbf{m}}{\partial t} + \nabla \cdot \left(\frac{\mathbf{m} \otimes \mathbf{m}}{\rho} \right) = -\nabla p + \nabla \cdot \tau \,, \tag{4}$$

$$\frac{\partial E}{\partial t} + \nabla \cdot \left(\frac{E\mathbf{m}}{\rho} \right) = -\nabla \cdot \left(\frac{p\mathbf{m}}{\rho} \right) + \nabla \cdot \left(\frac{\mathbf{m} \cdot \tau}{\rho} \right) - \nabla \cdot \mathbf{q} \,, \tag{5}$$

where the symbol $\otimes$ denotes the outer product, τ is the viscous stress and $\mathbf{q}$ is the heat flux, defined by

$$\tau = -2\mu \left(\nabla \mathbf{u} + (\nabla \mathbf{u})^{\mathrm{T}} \right) - \frac{2}{3}\mu \left(\nabla \cdot \mathbf{u} \right) \mathbf{I} \,, \tag{6}$$

$$\mathbf{q} = -\frac{\mu c_p}{\mathrm{Pr}} \nabla T \,, \tag{7}$$

where μ the dynamic viscosity, T is the temperature, c_p is the heat capacity at constant pressure, Pr is the Prandtl number and $\mathbf{I}$ is the identity matrix.

2.2. Complex differentiation method

To explain the complex differentiation method, the Taylor series of a function $f(\alpha)$ depending on a complex number $\alpha = \alpha_0 + ih$, where h is a real number, is considered. It can be written as:

$$f(\alpha_0 + ih) = f(\alpha_0) + ih \frac{\mathrm{d}f}{\mathrm{d}\alpha}(\alpha_0) - \frac{h^2}{2} \frac{\mathrm{d}^2 f}{\mathrm{d}\alpha^2}(\alpha_0) + O(h^3) \,. \tag{8}$$

In this formula, it can be noticed that approximate values of the function and its derivative at $\alpha = \alpha_0$ can be obtained, respectively by the real part of $f(\alpha_0 + ih)$ and from the imaginary part of $f(\alpha_0 + ih)$ as

$$\frac{\mathrm{d}f}{\mathrm{d}\alpha}(\alpha_0) = \frac{\mathrm{Im}\left[f(\alpha_0 + ih)\right]}{h} + O(h^2) \; . \tag{9}$$

The flow solutions and their derivatives with respect to a parameter can thus be estimated by carrying out a single simulation in which a small imaginary part is introduced to the parameter of interest.

2.3. Complex Navier-Stokes equations and sensitivity equations

Since the parameter under study should contain an imaginary part in the complex differentiation method, the other flow variables are also complex numbers and the Navier-Stokes equations are solved in a complex form. In the following, the flow variables are split into real and imaginary parts using the subscripts r and i. For example, the density can be written as

$$\rho = \rho_r + i\rho_i \; . \tag{10}$$

where ρ_r is the real part and ρ_i is the imaginary part of the density. By decomposing the Navier-Stokes equations into real and imaginary parts, two systems of equations are obtained. The first one describes the evolution of the real parts of flow variables and the second one their imaginary parts. These systems can be written as

$$\frac{\partial \rho_r}{\partial t} + \nabla \cdot \mathbf{m}_r = 0 \; , \tag{11}$$

$$\frac{\partial \mathbf{m}_r}{\partial t} + \nabla \cdot \left[\frac{\rho_r \left(\mathbf{m}_r \otimes \mathbf{m}_r - \mathbf{m}_i \otimes \mathbf{m}_i\right) + \rho_i \left(\mathbf{m}_r \otimes \mathbf{m}_i + \mathbf{m}_r \otimes \mathbf{m}_i\right)}{\rho_r^2 + \rho_i^2} \right] = -\nabla p_r + \nabla \cdot \tau_r \; , \tag{12}$$

$$\begin{aligned} \frac{\partial E_r}{\partial t} + \nabla \cdot \left[\frac{\rho_r \left(E_r \mathbf{m}_r - E_i \mathbf{m}_i\right) + \rho_i \left(E_r \mathbf{m}_i + E_i \mathbf{m}_r\right)}{\rho_r^2 + \rho_i^2} \right] = & - \nabla \cdot \left[\frac{\rho_r \left(p_r \mathbf{m}_r - p_i \mathbf{m}_i\right) + \rho_i \left(p_r \mathbf{m}_i + p_i \mathbf{m}_r\right)}{\rho_r^2 + \rho_i^2} \right] \\ & + \nabla \cdot \left[\frac{\rho_r \left(\mathbf{m}_r \cdot \tau_r - \mathbf{m}_i \cdot \tau_i\right) + \rho_i \left(\mathbf{m}_r \cdot \tau_i + \mathbf{m}_i \cdot \tau_r\right)}{\rho_r^2 + \rho_i^2} \right] \\ & - \nabla \cdot \mathbf{q}_r \; , \end{aligned} \tag{13}$$

and

$$\frac{\partial \rho_i}{\partial t} + \nabla \cdot \mathbf{m}_i = 0 \; , \tag{14}$$

$$\frac{\partial \mathbf{m}_i}{\partial t} + \nabla \cdot \left[\frac{\rho_r \left(\mathbf{m}_r \otimes \mathbf{m}_i + \mathbf{m}_i \otimes \mathbf{m}_r\right) + \rho_i \left(\mathbf{m}_i \otimes \mathbf{m}_i - \mathbf{m}_r \otimes \mathbf{m}_r\right)}{\rho_r^2 + \rho_i^2} \right] = -\nabla p_i + \nabla \cdot \tau_i \; , \tag{15}$$

$$\begin{aligned} \frac{\partial E_i}{\partial t} + \nabla \cdot \left[\frac{\rho_r \left(E_r \mathbf{m}_i + E_i \mathbf{m}_r\right) + \rho_i \left(E_i \mathbf{m}_i - E_r \mathbf{m}_r\right)}{\rho_r^2 + \rho_i^2} \right] = & - \nabla \cdot \left[\frac{\rho_r \left(p_r \mathbf{m}_i + p_i \mathbf{m}_r\right) + \rho_i \left(p_i \mathbf{m}_i - p_r \mathbf{m}_r\right)}{\rho_r^2 + \rho_i^2} \right] \\ & + \nabla \cdot \left[\frac{\rho_r \left(\mathbf{m}_r \cdot \tau_i + \mathbf{m}_i \cdot \tau_r\right) + \rho_i \left(\mathbf{m}_i \cdot \tau_i - \mathbf{m}_r \cdot \tau_r\right)}{\rho_r^2 + \rho_i^2} \right] \\ & - \nabla \cdot \mathbf{q}_i \; . \end{aligned} \tag{16}$$

Assuming that the order of magnitude of the real parts of the variables is much larger than that of their imaginary parts, the products of imaginary variables can be neglected. The real part of the complex Navier-Stokes equations can then be rewritten as

$$\frac{\partial \rho_r}{\partial t} + \nabla \cdot \mathbf{m}_r = 0 \; , \tag{17}$$

$$\frac{\partial \mathbf{m}_r}{\partial t} + \nabla \cdot \left(\frac{\mathbf{m}_r \otimes \mathbf{m}_r}{\rho_r} \right) = -\nabla p_r + \nabla \cdot \tau_r \ , \tag{18}$$

$$\frac{\partial E_r}{\partial t} + \nabla \cdot \left(\frac{E_r \mathbf{m}_r}{\rho_r} \right) = -\nabla \cdot \left(\frac{p_r \mathbf{m}_r}{\rho_r} \right) + \nabla \cdot \left(\frac{\mathbf{m}_r \cdot \tau_r}{\rho_r} \right) - \nabla \cdot \mathbf{q}_r \ , \tag{19}$$

giving equations identical to the real Navier-Stokes equations. In the same way, the imaginary part of the complex Navier-Stokes equations can be rewritten as

$$\frac{\partial \rho_i}{\partial t} + \nabla \cdot \mathbf{m}_i = 0 \ , \tag{20}$$

$$\frac{\partial \mathbf{m}_i}{\partial t} + \nabla \cdot \left[\frac{(\mathbf{m}_r \otimes \mathbf{m}_i + \mathbf{m}_i \otimes \mathbf{m}_r)}{\rho_r} - \frac{\rho_i \mathbf{m}_r \otimes \mathbf{m}_r}{\rho_r^2} \right] = -\nabla p_i + \nabla \cdot \tau_i \ , \tag{21}$$

$$\begin{aligned} \frac{\partial E_i}{\partial t} + \nabla \cdot \left[\frac{(E_r \mathbf{m}_i + E_i \mathbf{m}_r)}{\rho_r} - \frac{\rho_i E_r \mathbf{m}_r}{\rho_r^2} \right] = & -\nabla \cdot \left[\frac{(p_r \mathbf{m}_i + p_i \mathbf{m}_r)}{\rho_r} - \frac{\rho_i p_r \mathbf{m}_r}{\rho_r^2} \right] \\ & + \nabla \cdot \left[\frac{(\mathbf{m}_r \cdot \tau_i + \mathbf{m}_i \cdot \tau_r)}{\rho_r} - \frac{\rho_i \mathbf{m}_r \cdot \tau_r}{\rho_r^2} \right] - \nabla \cdot \mathbf{q}_i \ . \end{aligned} \tag{22}$$

The sensitivity equations are obtained by replacing the imaginary variables by the derivatives of the flow variables in the imaginary part of the complex Navier-Stokes equations. They describe the evolution of the derivatives of the flow variables with respect to a parameter. They can be written as

$$\frac{\partial \rho'}{\partial t} + \nabla \cdot \mathbf{m}' = 0 \ , \tag{23}$$

$$\frac{\partial \mathbf{m}'}{\partial t} + \nabla \cdot \left(\frac{\mathbf{m}' \otimes \mathbf{m} + \mathbf{m} \otimes \mathbf{m}'}{\rho} - \frac{\rho' \mathbf{m} \otimes \mathbf{m}}{\rho^2} \right) = -\nabla p' + \nabla \cdot \tau' \ , \tag{24}$$

$$\begin{aligned} \frac{\partial E'}{\partial t} + \nabla \cdot \left(\frac{E' \mathbf{m} + E \mathbf{m}'}{\rho} - \frac{\rho' E \mathbf{m}}{\rho^2} \right) = & -\nabla \cdot \left(\frac{p' \mathbf{m} + p \mathbf{m}'}{\rho} - \frac{\rho' p \mathbf{m}}{\rho^2} \right) \\ & + \nabla \cdot \left(\frac{\mathbf{m}' \cdot \tau + \mathbf{m} \cdot \tau'}{\rho} - \frac{\rho' \mathbf{m} \cdot \tau}{\rho^2} \right) - \nabla \cdot \mathbf{q}' \ , \end{aligned} \tag{25}$$

where the prime notation denotes derivatives. If the order of magnitude of the imaginary parts is much smaller than that of the real parts, the imaginary parts of the flow variables therefore follow the same spatio-temporal evolution as the derivatives of the flow variables. In order to estimate the flow solutions and sensitivities at the same time, it is thus only necessary to define as complex numbers the variables in a computational code dealing only with real numbers and to use complex arithmetic. Because of this, the implementation of the complex differentiation method in an in-house solver is straightforward.

3. Mixing layer parameters

The mixing layer configuration is similar to that considered in the simulations of Colonius *et al.* [18], Bogey *et al.* [19] and Moser *et al.* [20]. For illustration purpose, the mean streamwise velocity profile and snapshots of vorticity and pressure are presented in Figure 1. The streamwise component of the velocity imposed at the inlet boundary at $x = 0$ is given by the hyperbolic tangent profile

$$u_0(y) = U_c - \frac{\Delta U}{2} \tanh \left(\frac{2y}{\delta_\omega} \right) \ , \tag{26}$$

where $U_c = (U_1 + U_2)/2$ is the velocity at the center of the mixing layer, $\Delta U = U_2 - U_1$ is the velocity difference and $\delta_\omega = \Delta U / \max \left(|\mathrm{d}u_0/\mathrm{d}y| \right)$ is the vorticity thickness, at the inlet. The velocities of the slow and fast flows are given

by $U_1 = U_c - \Delta U/2$ and $U_2 = U_c + \Delta U/2$. At the inlet, temperature is fixed at $T_0 = 293\,\mathrm{K}$, pressure at $p_0 = 10^5\,\mathrm{Pa}$ and density is evaluated from the ideal gas law. Molecular viscosity is expressed as a function of temperature using Sutherland's law. The thermal conductivity λ is determined from the Prandtl number $\mathrm{Pr} = \mu c_p/\lambda = 0.75$, where $\mu = \nu\rho$ and ν is the kinematic viscosity. The value of 1.4 is considered for the adiabatic index γ. The Reynolds number based on the velocity difference is given by $\mathrm{Re}_\omega = \delta_\omega \Delta U/\nu$. The Mach number is defined by $\mathrm{M} = \Delta U/c_0$, where $c_0 = \sqrt{\gamma p_0/\rho_0}$ is the speed of sound in the ambient medium.

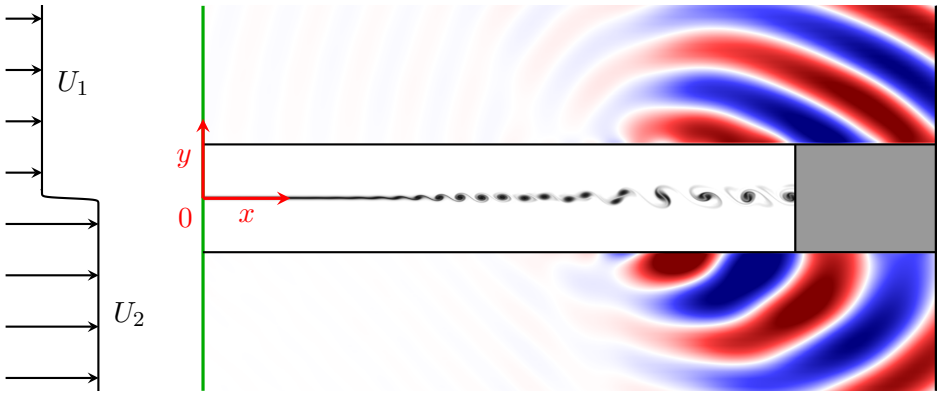

Figure 1: Schematic view of the mixing layer. Instantaneous vorticity and fluctuating pressure fields are represented at the center and on the periphery of the shear zone. The mean velocity profile is plotted on the left not to scale. The upstream boundary is represented by a green line. The sponge zone is in grey. Only a part of the computational domain is shown.

The aerodynamic development of the mixing layer is controlled by an excitation to focus on the acoustic radiation produced by the first stage of vortex pairings. The mixing layer is excited at a frequency f_0 and at the first subharmonic $f_0/2$ by introducing vortical disturbances at the center of the shear zone near the upstream boundary at $x = 10\delta_\omega$. The frequency f_0, given by the Strouhal number $\mathrm{St}_\omega = f_0 U_c/\delta_\omega = 0.132$, is close to the frequency of the most amplified instability waves developing in the velocity profile (26) [21]. More information on the excitation procedure can be found in Bogey *et al.* [19]. The flow development and the acoustic radiation of the mixing layer obtained by the excitation procedure detailed above are illustrated in Figure 1. Vortices form in the center of the shear zone due to the amplification and saturation of the amplitude of instability waves downstream of the upstream boundary. Subsequently, vortex pairings occur at the frequency $f_0/2$ and at a fixed location. These pairings produce acoustic waves which can be observed in Figure 1 on each side of the shear zone.

3.1. Simulation parameters

Three sets of simulations were carried out considering different Mach and Reynolds numbers, and several meshes. They are referred to as set-Mach, set-Reynolds and set-Mesh. The values of the Mach and Reynolds numbers, of the transverse mesh spacing at the center of the mixing layer, and the numbers of points in the streamwise and transverse directions n_x and n_y are given in Table 1. In set-Mach, mixing layers at Mach numbers M = 0.2, 0.25, 0.3, 0.35 and 0.4 with $U_c = 0.5c_0$ were considered. If the excitation frequency f_0 varies with the Mach number, the derivatives of the flow variables with respect to the Mach number, estimated using the complex differentiation method, are likely to increase with time because the derivative of a sine wave with respect to its frequency increases

with time. This increase makes it difficult to accurately estimate the derivatives of time-averaged variables. To compute the derivatives of acoustic variables with respect to the Mach number, the excitation frequency f_0 is thus set to $f_0 = \mathrm{St}_\omega U_c/\delta_\omega$, where $\delta_\omega = \mathrm{Re}_\omega \nu/\Delta U$, assuming a Reynolds number of 2000 and a velocity difference of $0.2c_0$, in the simulations of set-Mach. Therefore, the Reynolds number increases with the Mach number in set-Mach. As a result of this, the derivatives obtained with the complex differentiation method can be compared in a relevant way with the results of the parametric study.

In the simulations of set-Reynolds, mixing layers at Reynolds numbers Re_ω = 400, 800, 1600, 3200, 6400 and 12800, with M = 0.3 and $U_c = 0.5c_0$, were considered. A simulation of a mixing layer at a Reynolds number of 10^{12} which can be assumed as non-viscous was also performed. In these cases, the inlet vorticity thickness is provided by the Reynolds number.

In all cases mentioned above, the mesh spacing in the transverse direction at the center of the shear layer is $\Delta y_0 = 0.1\delta_\omega$. To investigate the grid sensitivity of the flow solutions, four simulations of mixing layers at a Reynolds number of 3000, with M = 0.3 and $U_c = 0.5c_0$, were carried out on grids with mesh spacings $\Delta y_0 = 0.1\delta_\omega$, $0.2\delta_\omega$, $0.4\delta_\omega$, and $0.8\delta_\omega$. They constitute the simulations set-Mesh.

The unsteady pressure have been recorded in the entire computational domain at a sampling frequency of $20f_0$ for set-Mach, $10f_0$ for set-Reynolds, and $20f_0$ for set-Mesh, after a transient period of more than $300T_p$, where $T_p = 2/f_0$ is the vortex pairing period. In all cases, the recording time is equal to $10T_p$.

3.2. Numerical methods

The direct numerical simulations are carried out with an in-house code [19] which solves the unsteady compressible Navier-Stokes equations in Cartesian coordinates (x, y) using low-dissipation and low-dispersion explicit schemes. Fourth-order eleven-point centered finite differences are used for spatial discretization. A second-order six-stage Runge-Kutta algorithm is implemented for time integration [22]. To remove grid-to-grid oscillations without affecting the wavenumbers accurately resolved, a sixth-order eleven-point centered filter [23] is applied explicitly to the flow variables at the end of each time step. Non-centered finite differences and filters are used near the grid boundaries [24]. The radiation conditions of Tam & Dong [25] are applied at the boundaries to avoid significant spurious reflections. A sponge zone combining mesh stretching, Laplacian filtering and a procedure to keep the mean values of density and pressure around their ambient values is implemented at the downstream boundary.

3.3. Computational parameters

Domains of length $L_x = 1200\delta_\omega$ and width L_y varying from $400\delta_\omega$ to $1200\delta_\omega$ are used. In set-Mach and set-Reynolds, the mesh spacing in the transverse direction at the center of the mixing layer is equal to $\Delta y_0 = 0.1\delta_\omega$. From $y = 0$, it is stretched on both sides of the mixing layer at a rate of 4% until it reaches a length of $\Delta y \simeq 5\delta_\omega$ at $y = \pm 124\delta_\omega$ and then is constant until $y = \pm L_y/2$, where $L_y = 400\delta_\omega$. In set-Mesh, the transverse mesh spacing at the center of the mixing layer is equal to $0.1\delta_\omega$, $0.2\delta_\omega$, $0.4\delta_\omega$ or $0.8\delta_\omega$. It is stretched on both sides of the mixing layer at a rate of 2% until $y = \pm L_y/2$, where $L_y = 1200\delta_\omega$.

At the inlet, the mesh spacing in the streamwise direction is equal to $\Delta x_0 = 0.2\delta_\omega$. It is constant down to $x = x_{\mathrm{sz}}$, where x_{sz} is the position of the beginning of the sponge zone, then increases at a rate of 2% down to

Table 1: Mixing layer parameters for the three sets of simulations referred to as set-Mach, set-Reynolds and set-Mesh: Mach number $M = \Delta U/c_0$, Reynolds number $Re_\omega = \delta_\omega \Delta U/\nu$, transverse mesh spacing at the center of the mixing layer Δy_0, numbers of points in the streamwise and transverse directions n_x and n_y.

Set	M	Re_ω	$\Delta y_0/\delta_\omega$	n_x	n_y
set-Mach	0.2	2000	0.1	1731	235
	0.25	2500		1435	
	0.3	3000		1286	
	0.35	3500		1237	
	0.4	4000		1138	
set-Reynolds	0.3	400	0.1	1286	235
		800			
		1600			
		3200			
		6400			
		12800			
		10^{12}			
set-Mesh	0.3	3000	0.1	1286	491
			0.2		419
			0.4		349
			0.8		283

Table 2: Sponge zone parameters: Mach number M, position of the beginning of the sponge zone $x_{\rm sz}$, and length x_σ along which the intensity of the Laplacian filter increases.

M	0.2	0.25	0.3	0.35	0.4
$x_{\rm sz}/\delta_\omega$	300	240	210	200	180
x_σ/δ_ω	200	200	150	150	100

$x = L_x$. In the sponge zone, a Laplacian filter is applied to density, velocity, and pressure fluctuations. Its intensity $\sigma_{\rm sz}$ is given by

$$\sigma_{\rm sz}(x,y) = \begin{cases} \sigma_{\max}\left(\dfrac{x-x_{\rm sz}}{x_\sigma}\right)\exp\left(-\ln(2)\dfrac{y^2}{b_{\rm sz}^2}\right) & \text{for } x_{\rm sz} < x \le x_{\rm sz}+x_\sigma\ , \\ \sigma_{\max}\exp\left(-\ln(2)\dfrac{y^2}{b_{\rm sz}^2}\right) & \text{for } x > x_{\rm sz}+x_\sigma\ , \end{cases} \tag{27}$$

where $\sigma_{\max} = 0.2$ and x_σ is a length varying between $100\delta_\omega$ and $200\delta_\omega$. A Gaussian function of half thickness $b_{\rm sz} = 3\delta_\omega$ centered at $y = 0$ is introduced to avoid that the Laplacian filter affects the acoustic waves produced by the vortex pairings outside the shear-flow.

The velocity difference $\Delta U = U_2 - U_1$ increases with the Mach number, hence the velocity ratio $R = \Delta U/(2U_c)$ also increases. Monkewitz and Huerre [21] have shown using linear stability analyses that the growth rates of the instability waves developing near the inlet are proportional to the velocity ratio. Therefore, vortex pairings are expected to be located further upstream as the Mach number increases. To isolate the acoustic radiation produced by the pairings, the position of the beginning of the sponge zone $x_{\rm sz}$ thus varies in the simulations. The length x_σ along which the intensity of the Laplacian filter increases is also adjusted. The values considered for $x_{\rm sz}$ and x_σ are given in Table 2, depending on the Mach number. The position of the beginning of the sponge zone decreases from $x_{\rm sz} = 300\delta_\omega$ for M = 0.2 down to $x_{\rm sz} = 180\delta_\omega$ for M = 0.4 and the length x_σ decreases from $x_\sigma = 200\delta_\omega$ for M = 0.2 down to $x_\sigma = 100\delta_\omega$ for M = 0.4. To ensure the stability of the simulations in all cases, the time step is set to $\Delta t = 0.9\Delta y_{\rm CFL}/c_0$, where $\Delta y_{\rm CFL} = 0.1\delta_\omega$.

4. Comparison between a first-order approximation and the complex differentiation method

In this section, the accuracies of a first-order approximation and the complex differentiation method are studied by estimating the derivative of the acoustic power of mixing layers at different Reynolds number with respect to the latter parameter. Mixing layers at $\mathrm{Re}_\omega = 400$, 3000 and 12800 that are expected to be strongly, weakly and very weakly sensitive to viscous effects have been considered to vary the value of the derivative of interest and thus to be able to investigate the influence of the magnitude of this derivative on the accuracy of each method. In each case, the Mach number is equal to 0.3, U_c is equal to $0.5c_0$, the inlet vorticity thickness is determined from the Reynolds number, and the grid is the same as in the simulations of set-Mach and set-Reynolds.

Using the first-order approximation, the derivative is computed by performing two DNS, one for a value of the viscosity $\nu_0 = \delta_\omega\Delta U/\mathrm{Re}_\omega$ and another one for $\nu = \nu_0(1+h)$, where h is a real number denoting a perturbation magnitude, and by applying the formula

$$\frac{\mathrm{d}W}{\mathrm{dRe}_\omega} = \frac{\mathrm{d}W}{\mathrm{d}\nu}\frac{\mathrm{d}\nu}{\mathrm{dRe}_\omega} \simeq -\frac{W\left(\nu_0\left(1+h\right)\right) - W\left(\nu_0\right)}{h\mathrm{Re}_\omega}\ , \tag{28}$$

where W is the acoustic power estimated by integrating the sound intensity over circles of radius $r = 200\delta_\omega$ centered on the vortex pairings. Using the complex differentiation method, the derivative is estimated by performing a DNS with a viscosity $\nu = \nu_0 (1 + ih)$ and from the imaginary part of the acoustic power by

$$\frac{\mathrm{d}W}{\mathrm{dRe}_\omega} \simeq -\frac{\mathrm{Im}\left[W\left(\nu_0\left(1+ih\right)\right)\right]}{h\mathrm{Re}_\omega} \ . \tag{29}$$

To investigate the influence of the perturbation magnitude h on the accuracy of the first-order approximation and the complex differentiation method, simulations have been carrying out for values of h ranging from 10^{-10} to 1. In each case, the relative error, defined as

$$\mathrm{Err}\left(h\right) = \frac{\left| \dfrac{\mathrm{d}W}{\mathrm{dRe}_\omega}\left(h\right) - \dfrac{\mathrm{d}W}{\mathrm{dRe}_\omega}^{\mathrm{ref}} \right|}{\dfrac{\mathrm{d}W}{\mathrm{dRe}_\omega}^{\mathrm{ref}}} \ , \tag{30}$$

where $\mathrm{d}W/\mathrm{dRe}_\omega{}^{\mathrm{ref}}$ is a reference value estimated by applying the complex differentiation method with $h = 10^{-100}$, has been evaluated. The reference values computed for $\mathrm{Re}_\omega = 400$, 3000 and 12800 are not given for brevity but their variations with the Reynolds number are described in the following. They decrease with the Reynolds number, indicating that the acoustic power of the mixing layer is less sensitive to viscous effects as the Reynolds number increases, as expected. For instance, for $\mathrm{Re}_\omega = 400$, the reference value is almost 20 times higher than the one determined for $\mathrm{Re}_\omega = 12800$. For $h = 10^{-1}$ and $h = 1$, the simulations performed with the complex differentiation method have diverged due to numerical instabilities increasing with time. These instabilities develop earlier as the value of h increases, which suggests that they are related to the effects of the imaginary parts of the flow variables on their real parts. Indeed, if the order of magnitude of the imaginary part of the flow variables is close to or greater than that of the real part of the latter, the products of imaginary variables can no longer be neglected in the real parts of the complex Navier-Stokes equations and the latter equations are therefore no longer an accurate approximation of the Navier-Stokes equations.

The relative errors obtained for $\mathrm{Re}_\omega = 400$, 3000 and 12800 are plotted in Figures 2(a), 2(b) and 2(c) as a function of the perturbation magnitude h using a logarithmic scale. The values calculated for the first-order approximation and for the complex differentiation method are displayed. Lines corresponding to the leading terms of the truncation error of the two approaches, varying according to h and h^2, are also plotted. In all cases, the error obtained using the complex differentiation method is smaller than that of the first-order approximation, showing that the first method is more accurate than the second one. For $\mathrm{Re}_\omega = 400$ in Figure 2(a), the error determined by the two methods is reduced as the perturbation magnitude h decreases from $h = 1$ to $h = 10^{-5}$. For this range of h, the error varies as the truncation errors of the two methods. As h decreases from 10^{-5} to 10^{-10}, the error obtained using the first-order approximation increases as the inverse of h. This result indicates that the values of $W(\nu(1 + h))$ with $h \leq 10^{-5}$ and $W(\nu)$ are so close that their difference is of the order of the round-off errors, in agreement with results obtained by Anderson *et al.* [8]. The error evaluated using the complex differentiation method does not vary significantly between $h = 10^{-5}$ and $h = 10^{-10}$. For $\mathrm{Re}_\omega = 3000$ and $\mathrm{Re}_\omega = 12800$ in Figures 2(b,c), the variations of the errors with h estimated using the first-order approximation and the complex differentiation method are similar to those obtained for $\mathrm{Re}_\omega = 400$. This indicates that the accuracy of the complex

Table 3: CPU time to perform one temporal iteration and memory needed for a simulation with and without the complex differentiation method.

	CPU time [s]	Memory [Mb]
without CDM	0.200	89.8
with CDM	0.406	167

differentiation method does not depend on the perturbation magnitude h for $h < 10^{-5}$ for the three values of the Reynolds number considered. Since the reference value of the derivative of the acoustic power decreases with the Reynolds number, the results also suggest that the accuracy of the complex differentiation method is not affected by the magnitude of the derivative of interest. Similar results, not shown her for brevity, were obtained for mixing layers at Mach numbers equal to 0.2 and 0.4, and considering grids with mesh spacings $\Delta y_0 = 0.2\delta_\omega$ and $0.4\delta_\omega$. Therefore, the perturbation magnitude h is set to 10^{-5} in the following sections.

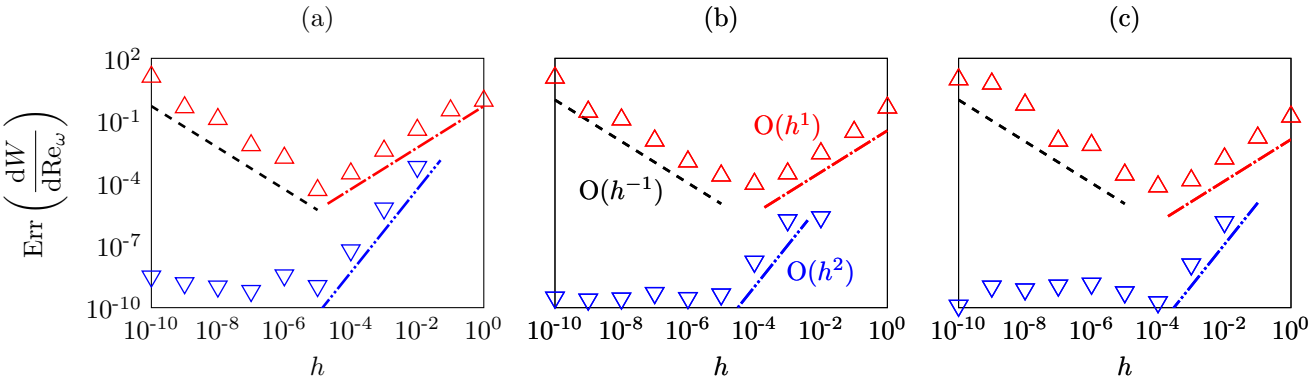

Figure 2: Variations of the relative error on the derivative of the acoustic power with respect to the Reynolds number with the perturbation magnitude h obtained with △ a first-order approximation and ▽ the complex differentiation method for (a) $\mathrm{Re}_\omega = 400$, (b) $\mathrm{Re}_\omega = 3000$ and (c) $\mathrm{Re}_\omega = 12800$, and variations of the order of magnitude of the truncation error of —·— the first-order approximation and —··— the complex differentiation method.

To compare the numerical cost of the complex differentiation method with that of the first-order approximation, the CPU time to perform one temporal iteration and the memory required for simulations carried out with and without the complex differentiation method are reported in Table 3. The CPU time is doubled and the memory increases by 85% when the complex differentiation method is used. These results can be expected to vary with the computer and the code used. For comparison, Martins *et al.* [26] reported factors of 2.2 to 4.8 between the time of simulations with and without the complex differentiation method using various computing platforms, and Anderson *et al.* [8] indicated a doubling of the memory required when the complex differentiation method is implemented.

5. Sensitivity analysis using the complex differentiation method

5.1. Mach number sensitivity

In each of the simulations of set-Mach, the complex differentiation method is implemented to estimate the derivatives of acoustic variables with respect to the Mach number. For this purpose, a small imaginary perturbation ih

is introduced in the formula (26) of the inlet velocity profile

$$u_0(y) = U_c - \frac{\Delta U}{2}(1+ih)\tanh\left(\frac{2y}{\delta_\omega}\right) . \tag{31}$$

An approximate value of the derivative of a function f with respect to the Mach number can then be determined from the imaginary part of f by

$$\frac{\mathrm{d}f}{\mathrm{dM}} \simeq \frac{\mathrm{Im}\,[f]}{h\mathrm{M}} . \tag{32}$$

Therefore, the imaginary part of f provides information on the sensitivity of the function f to the Mach number. A small perturbation is added to the velocity difference ΔU in equation (31), but since the inlet vorticity thickness δ_ω is fixed, the Reynolds number $\mathrm{Re}_\omega = \delta_\omega \Delta U/\nu$ is also influenced by the perturbation. The imaginary part of f is thus also linked to the effects of the Reynolds number on f. However, the influence of the viscosity on the flow variables is weak for a high Reynolds number flow, which is the case for the mixing layers of set-Mach with $\mathrm{Re}_\omega \geq 2000$. Therefore, the imaginary part of f is mainly associated with the Mach number sensitivity.

5.2. Reynolds number sensitivity

In the simulations of set-Reynolds, the viscosity is set to $\nu(1+ih)$. In this way, the derivative of a function f with respect to the Reynolds number is linked to the imaginary part of f by

$$\frac{\mathrm{d}f}{\mathrm{dRe}_\omega} = \frac{\mathrm{d}f}{\mathrm{d}\nu}\frac{\mathrm{d}\nu}{\mathrm{dRe}_\omega} \simeq -\frac{\mathrm{Im}\,[f]}{h\mathrm{Re}_\omega} . \tag{33}$$

Thus, the imaginary part of f provides information on the sensivity of f to the Reynolds number.

5.3. Grid sensitivity

To study the influence of the grid resolution on the flow solutions, the transverse mesh spacing at the center of the mixing layer is set to $\Delta y_0(1+ih)$ in each simulation of set-Mesh. An approximate value of the derivative of a function f with respect to Δy_0 can then be estimated at nodes y_i. This derivative can be written as

$$\frac{\mathrm{d}f}{\mathrm{d}\Delta y_0}(y_i) = \lim_{\epsilon\to 0}\frac{f(\Delta y_0+\epsilon, y_i(\Delta y_0+\epsilon)) - f(\Delta y_0, y_i(\Delta y_0))}{\epsilon} , \tag{34}$$

where ϵ is a real number. This derivative can be obtained from the imaginary part of f by

$$\frac{\mathrm{d}f}{\mathrm{d}\Delta y_0}(y_i) \simeq \frac{\mathrm{Im}\,[f]}{h\Delta y_0}(y_i) . \tag{35}$$

In the right hand side of the definition (34), the function f evaluated at a given node y_i but at two different positions: $y = y_i(\Delta y_0+\epsilon)$ and $y = y_i(\Delta y_0)$. The derivative obtained from the difference between $f(\Delta y_0+\epsilon, y_i(\Delta y_0+\epsilon))$ and $f(\Delta y_0, y_i(\Delta y_0))$ thus does not indicate the effects of a small modification of the mesh spacing Δy_0 on the values of the function f computed at a given location y. Indeed, these effects are provided by the partial derivative

$$\frac{\partial f}{\partial \Delta y_0}(y_i) = \lim_{\epsilon\to 0}\frac{f(\Delta y_0+\epsilon, y_i) - f(\Delta y_0, y_i)}{\epsilon} , \tag{36}$$

which is defined from the difference between $f(\Delta y_0+\epsilon)$ and $f(\Delta y_0)$ obtained at the same location $y = y_i(\Delta y_0)$. This derivative can be estimated using the chain rule as follows

$$\frac{\partial f}{\partial \Delta y_0}(y_i) = \frac{\mathrm{d}f}{\mathrm{d}\Delta y_0}(y_i) - \frac{\partial f}{\partial y}(y_i)\frac{\mathrm{d}y}{\mathrm{d}\Delta y_0}(y_i) , \tag{37}$$

where $\mathrm{d}f/\mathrm{d}\Delta y_0$ is obtained from the imaginary part of f using the complex differentiation method and the formula (35), $\partial f/\partial y$ is evaluated by differentiating the real part of f with respect to the coordinate y, and $\mathrm{d}y/\mathrm{d}\Delta y_0$ is given by

$$\frac{\mathrm{d}y}{\mathrm{d}\Delta y_0}(y_i) = \begin{cases} \displaystyle\sum_{j=0}^{i} r_y^j & \text{for } i = 0, ..., (n_y - 1)/2, \\ \displaystyle -\sum_{j=0}^{-i-1} r_y^j & \text{for } i = -(n_y - 1)/2, ..., -1, \end{cases} \tag{38}$$

where $r_y = 1.02$ is the stretching rate in the transverse direction.

6. Results

6.1. Mach number sensitivity

To illustrate the effects of the Mach number on the aerodynamic development and acoustic radiation of the mixing layers, snapshots of vorticity and fluctuating pressure are provided in Figures 3(a-c) for the mixing layers at M = 0.2, 0.3 and 0.4 of set-Mach. In all cases and downstream of the inlet forcing, the amplitude of the perturbations in the shear zone increases with the streamwise direction and then saturates, leading to the formation of vortices at the frequency f_0. Subsequently, vortex pairings occur at the frequency $f_0/2$ as in the simulations carried out by Bogey *et al.* [19] and Moser *et al.* [20]. Vortex rolling-ups and pairings take place at fixed axial positions. They move upstream as the Mach number increases, because the shear layer is more unstable as the velocity ratio $R = \Delta U/(2U_c)$ increases [21]. For example, the vorticity sheet starts to roll up near $x = 100\delta_\omega$ for M = 0.2 and near $x = 60\delta_\omega$ for M = 0.4, and vortex pairings occur near $x = 225\delta_\omega$ for M = 0.2 and near $x = 125\delta_\omega$ for M = 0.4.

The pairings produce acoustic waves propagating on both sides of the mixing layers, as expected. The amplitude of the sound waves increases strongly with the Mach number. This result is consistent with dimensional analyses [27, 28] which have shown that the noise produced by a two-dimensional free flow is proportional to the seventh power of the Mach number. For $\theta = 90°$, where θ is the polar angle defined with the respect to the streamwise direction and by polar coordinates (r, θ) where $r = 0$ is the location of the vortex pairing, the wavelength of the sound waves is equal to $\lambda = c_0/(f_0/2) \simeq 30\delta_\omega$ in all cases. It is smaller upstream of the vortex pairings for $\theta > 90°$ and larger downstream for $\theta < 90°$ due to the effects of the mean flow on the acoustic wave propagation [29].

Sound directivities

To quantify the effects of Mach number on the noise radiation of the mixing layers, the acoustic intensity

$$I = \frac{{p'_{\mathrm{RMS}}}^2}{\rho_0^2 c_0^4}\ , \tag{39}$$

where p'_{RMS} is the root-mean-square (RMS) value of the pressure flucutations, has been evaluated on circles of radius $r = 200\delta_\omega$ centered on the vortex pairings. It is plotted for all Mach numbers as a function of the polar angle θ for $-120° \leq \theta \leq 120°$ in Figure 4 using a logarithmic scale. For all angles, except for $\theta = 0$, the levels increase with the Mach number. In addition, the noise radiation is less oriented downstream as the Mach number increases from 0.25 to 0.4. For example, the peak intensity in the slow flow region ($y > 0$) is reached at $\theta \simeq 15°$ for

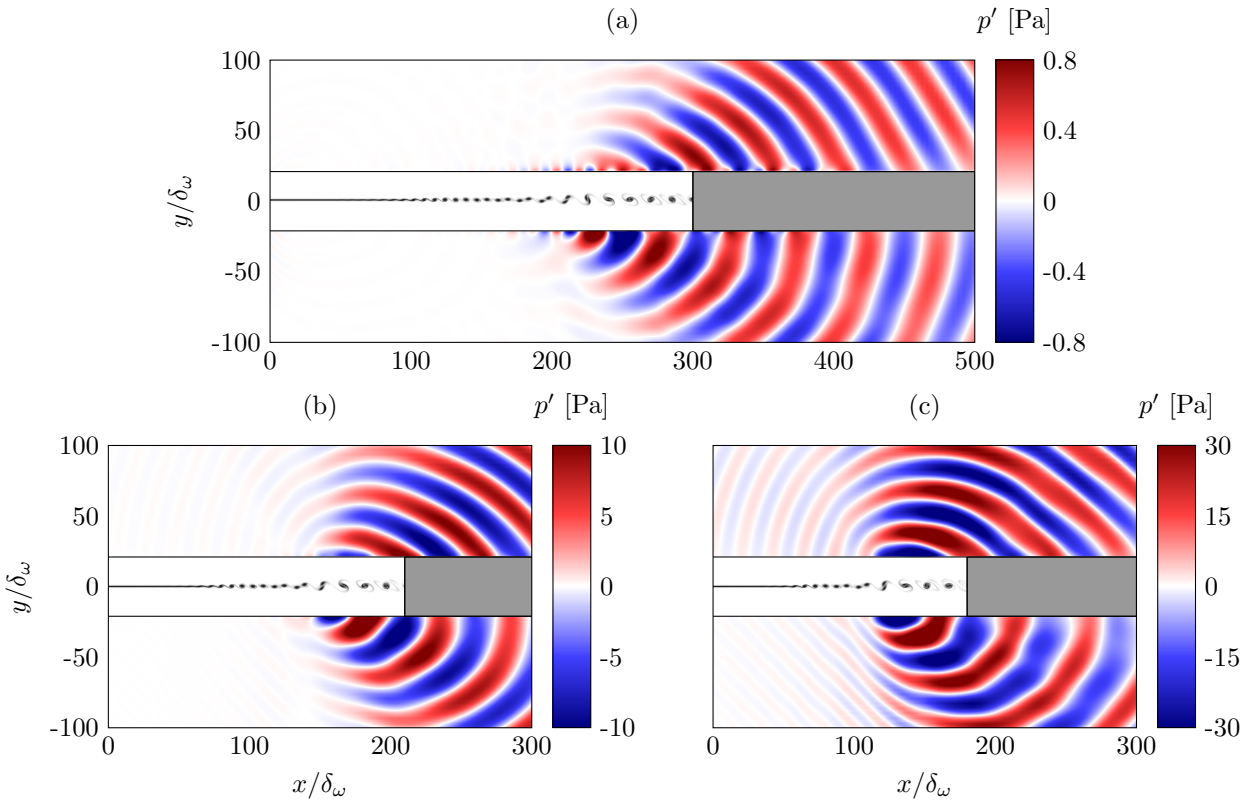

Figure 3: Instantaneous vorticity and fluctuating pressure fields for (a) M = 0.2, (b) M = 0.3 and (c) M = 0.4. The colour scale ranges from 0 to $\Delta U/\delta_\omega$ for vorticity, from white to black.

M = 0.25, $\theta \simeq 30°$ for M = 0.3 and $\theta \simeq 60°$ for M = 0.4. In order to explain this result, the fluctuating part of the Lighthill stress tensor [29] is considered without the viscous and entropy terms. It can be written as

$$\mathbf{T}' = \underbrace{\rho\langle\mathbf{u}\rangle \otimes \mathbf{u}' + \rho\mathbf{u}' \otimes \langle\mathbf{u}\rangle}_{\mathbf{T}^{\text{shear-noise}}} + \underbrace{\rho\mathbf{u}' \otimes \mathbf{u}'}_{\mathbf{T}^{\text{self-noise}}} , \tag{40}$$

where $\mathbf{T}^{\text{shear-noise}}$ and $\mathbf{T}^{\text{self-noise}}$ are linear and non-linear with respect to the velocity fluctuations $\mathbf{u}'$. The order of magnitude of the mean velocity vector corresponds to the inlet velocity at the center of the mixing layers, wich is $U_c = (U_1 + U_2)/2 = 0.5c_0$ and the order of magnitude of the vector of velocity fluctuations is the velocity difference $\Delta U = U_2 - U_1$. Therefore, the orders of magnitude of the tensors $\mathbf{T}^{\text{shear-noise}}$ and $\mathbf{T}^{\text{self-noise}}$ are given by

$$\mathbf{T}^{\text{shear-noise}} \sim \rho_0 U_c \Delta U , \tag{41}$$

$$\mathbf{T}^{\text{self-noise}} \sim \rho_0 \Delta U^2 . \tag{42}$$

As the Mach number $\mathrm{M} = \Delta U/c_0$ increases, the magnitude of the non-linear tensor $\mathbf{T}^{\text{self-noise}}$ thus increases more than the magnitude of the tensor $\mathbf{T}^{\text{shear-noise}}$. Ribner [30] by analytical developments and Freund [31] by analyzing a direct numerical simulation of a jet at M = 0.9 have shown that the acoustic radiation linked to the tensor $\mathbf{T}^{\text{shear-noise}}$ is more oriented downstream than the acoustic radiation linked to the tensor $\mathbf{T}^{\text{self-noise}}$. Therefore, the noise radiation produced by the mixing layers is less oriented downstream as the Mach number increases.

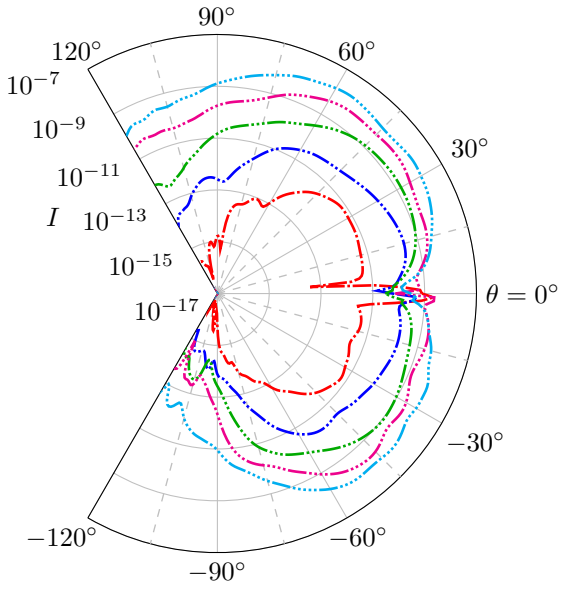

Figure 4: Variations of the acoustic intensity on circle of radius $r = 200\delta_\omega$ centered on the vortex pairings, as a function of the polar angle θ for M = 0.2, M = 0.25, M = 0.3, M = 0.35 and M = 0.4.

Sound intensities and their derivatives with respect to the Mach number

The RMS values of pressure fluctuations and their derivatives with respect to the Mach number, obtained using the complex differentiation method for M = 0.2, 0.3 and 0.4, are displayed in Figures 5(a,b,c) and 5(d,e,f). In all cases, the pressure fluctuations are strongest near the center of the mixing layers due to aerodynamic instability waves developing in the shear zone. In the acoustic fields, the sound levels are highest in two lobes pointing downstream and originating from the vortex-pairing location, as expected. In these lobes, the acoustic levels increase strongly with the Mach number. The lobes are oriented less downstream as the Mach number increases, in agreement with the dimensional analysis. Bands of low sound levels are observed downstream of the vortex pairings for M = 0.4 in Figure 5(c). Simulations of mixing layers at M = 0.4 carried out with sponge zones starting at different streamwise positions, not shown here for brevity, revealed that these bands are not related to sponge zone effects. Therefore, the bands may be due to interactions between the acoustic radiation produced by the vortex pairings and that of weaker noise sources located between the pairings and near the beginning of the sponge zone.

The derivatives of the pressure fluctuation levels with respect to the Mach number in Figures 5(d,e,f) are mostly positive in the acoustic field since the noise levels increase with this parameter. They are stronger as the Mach number increases. Therefore, they indicate that the noise levels increase more with the Mach number at high Mach numbers than at low Mach numbers, which is consistent with the seventh power law. In all cases, the derivatives are negative in narrow bands located downstream of the vortex pairings. Negative derivative values indicate that a small increase in the Mach number value leads to a reduction of the noise levels. The results thus suggest that the sound levels decrease with the Mach number in the narrow bands mentioned above. In these bands, the derivatives are higher, in absolute value, as the Mach number increases. This indicates that the noise levels in the bands are more sensitive to the Mach number effects as the latter parameter increases.

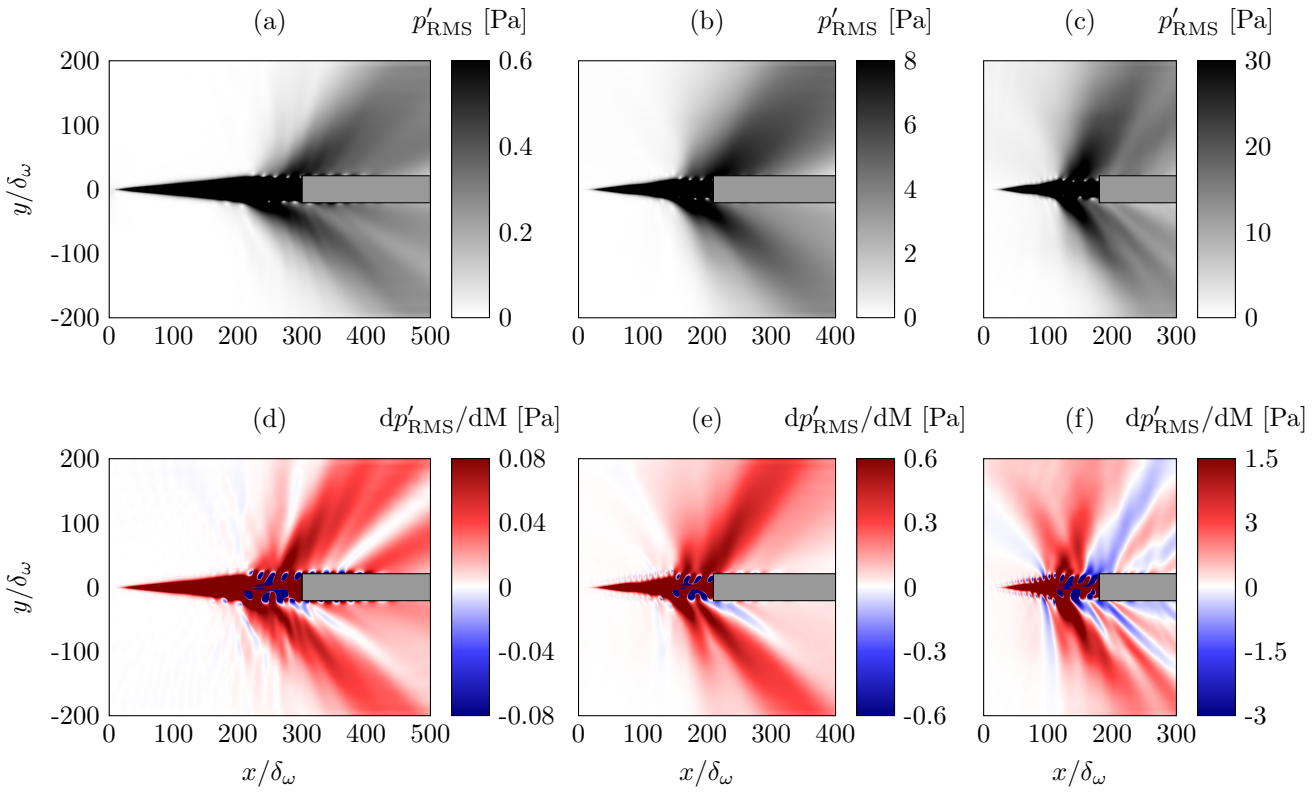

Figure 5: Fields of (a,b,c) the RMS values of pressure fluctuations and (d,e,f) their derivatives with respect to the Mach number for (a,d) M = 0.2, (b,e) M = 0.3 and (c,f) M = 0.4.

Dimensional law and acoustic power

The maximum values of the sound intensity at $r = 200\delta_\omega$ of the vortex-pairings location in the fast and slow flows of the mixing layers are compared with those found by Moser *et al.* [20] for two-dimensional mixing layers at Mach numbers between 0.2 and 0.4 computed by DNS. The mixing layers considered by Moser *et al.* [20] are at lower Reynolds number ($\mathrm{Re}_\omega = 400$) and are excited at lower frequencies than those in the present study. In addition, the velocity $U_c = (U_1 + U_2)/2$ is not the same in the two studies. The results from Moser *et al.* [20] and the present study are therefore expected to differ. In addition, in Moser *et al.* [20], the intensity was evaluated at $r = 300\delta_\omega$, whereas the calculation domain extends only to $y = 200\delta_\omega$ in the present study. Therefore, the intensity given by Moser *et al.* [20] has been approximated at $r = 200\delta_\omega$ by assuming the classical decay of the intensity in $1/r$ for a two-dimensional flow. The maximum values thus obtained are plotted as a function of the Mach number in Figure 6(a) using a logarithmic scale. In both studies, the levels increase strongly with the Mach number. For all Mach numbers, the values obtained by Moser *et al.* [20] are higher than those in the present study. The agreement is better as the Mach number increases.

The effects of the Mach number on the sound power levels are now investigated. These levels are estimated from the acoustic power W evaluated over circles of radius $r = 200\delta_\omega$ centered on the vortex pairings, from $\theta = 5°$ to $\theta = 150°$ in the upper flow, and from $\theta = -150°$ to $\theta = -5°$ in the lower flow. They are defined by

$$L_W = 10 \log \left(\frac{W}{W_{\mathrm{ref}}} \right) , \tag{43}$$

where $W_{\text{ref}} = 10^{-12}\,\text{kg.m}^2\text{.s}^{-3}$. They are plotted in Figure 6 as a function of the Mach number using a logarithmic scale. A line indicating the seventh power law is also represented for comparison. The sound power levels increase strongly with the Mach number for $\text{M} < 0.3$ and more weakly thereafter. For $\text{M} \geq 0.3$, the increase is consistent with the seventh power of the Mach number, in good agreement with results obtained by Ffowcs-Williams [27] and Guo [28] using analytical developments and by Moser *et al.* [20] using DNS of two-dimensional mixing layers at Mach numbers between 0.2 and 0.4.

The derivatives of the power levels with respect to the Mach number were obtained using the complex differentiation method. They are represented in Figure 6 by red segments of arbitrarily chosen lengths. Their values increase with the Mach number for $\text{M} \leq 0.25$, decrease from $\text{M} = 0.25$ to $\text{M} = 0.3$ and does not seem to vary thereafter. The red segments follow the variations of the power levels. The derivatives of these levels with respect to the Mach number thus provide a good estimation of the sensitivity of the noise levels to the Mach number.

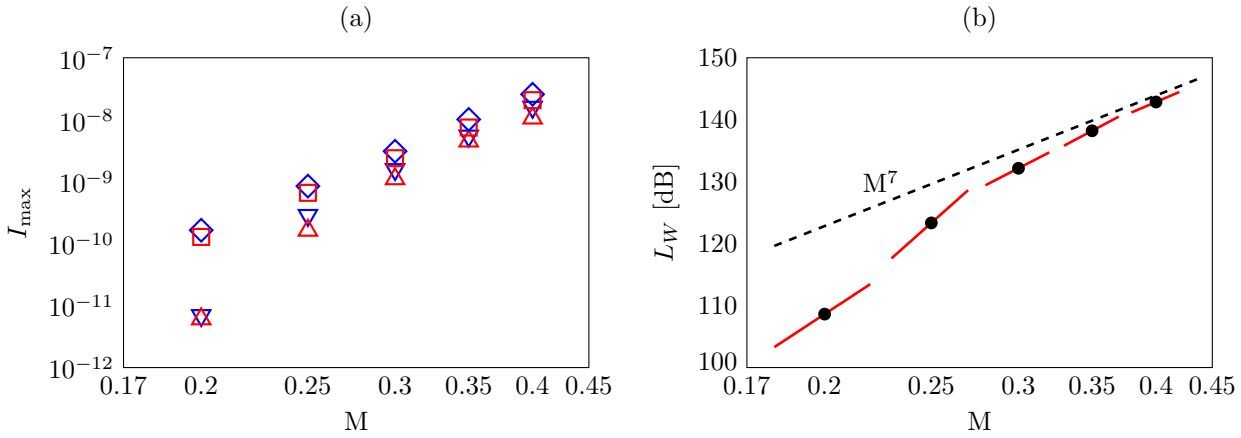

Figure 6: Variations of (a) the maximum intensity computed in the present study in the △ fast ($y < 0$) and ▽ slow ($y > 0$) flows of the mixing layers, and by Moser *et al.* [20] in the □ fast and ◇ slow flows, and (b) the acoustic power levels and ——— their derivatives with respect to the Mach number; - - - - - M^7 law.

6.2. Reynolds number sensitivity

Vorticity and pressure fields

Snapshots of vorticity and fluctuating pressure obtained from the simulations of set-Reynolds for $\text{Re}_\omega = 400$, 800, 1600, 3200, 6400 and 12800 are provided in Figures 7(a-f). In all cases, vortex rolling-ups and pairings occur. The pairings produce acoustic waves which propagate on both sides of the shear zone. The amplitudes of the sound waves increase with the Reynolds number. They increase strongly between $\text{Re}_\omega = 400$ and $\text{Re}_\omega = 800$, then more weakly between $\text{Re}_\omega = 800$ and $\text{Re}_\omega = 1600$, and not seem to vary significantly with the Reynolds number for $\text{Re}_\omega \geq 1600$. The acoustic radiation of the mixing layers is thus weakly dependent on viscous effects for $\text{Re}_\omega \geq 1600$. The wavelength of the sound waves does not vary with the Reynolds number and is equal to $\lambda = c_0/(f_0/2) \simeq 30\delta_\omega$ for a polar angle of 90°.

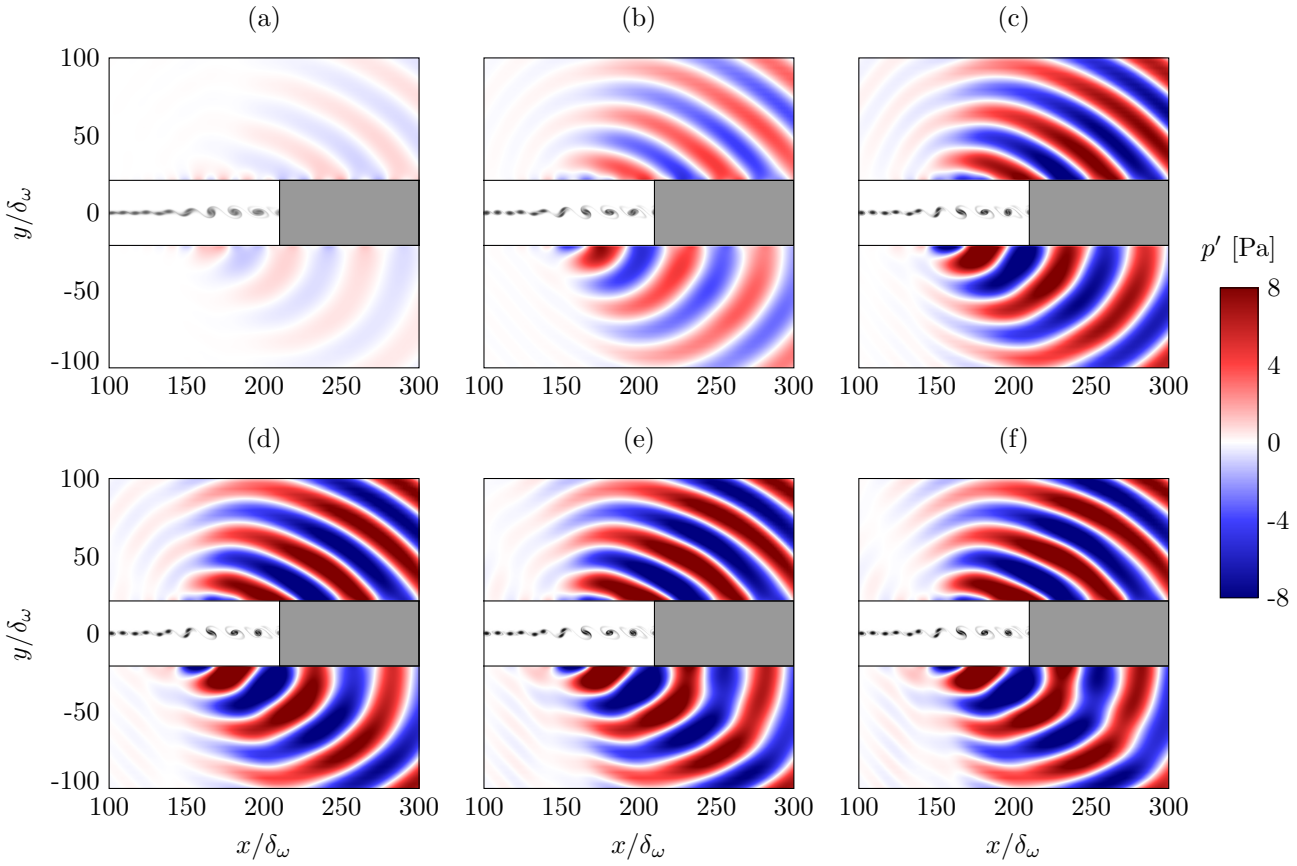

Figure 7: Instantaneous vorticity and fluctuating pressure fields for (a) $\mathrm{Re}_\omega = 400$, (b) $\mathrm{Re}_\omega = 800$, (c) $\mathrm{Re}_\omega = 1600$, (d) $\mathrm{Re}_\omega = 3200$, (e) $\mathrm{Re}_\omega = 6400$ and (f) $\mathrm{Re}_\omega = 12800$. The colour scale ranges from 0 to $\Delta U/\delta_\omega$ for vorticity, from white to black.

Sound directivities

The sound pressure levels obtained at $r = 200\delta_\omega$ from the vortex pairings for $\mathrm{Re}_\omega = 400$, 800, 1600, 3200 and 10^{12} are presented in Figure 8 for polar angles θ between $-120°$ and $120°$. For $\mathrm{Re}_\omega \leq 3200$, the levels increase with the Reynolds number downstream of the pairings, for $-90° < \theta < 90°$. The increase is less pronounced as the Reynolds number increases. It is strong between $\mathrm{Re}_\omega = 400$ and $\mathrm{Re}_\omega = 800$, moderate between $\mathrm{Re}_\omega = 800$ and $\mathrm{Re}_\omega = 1600$, and weak between $\mathrm{Re}_\omega = 1600$ and $\mathrm{Re}_\omega = 3200$. The values obtained for $\mathrm{Re}_\omega = 3200$ and $\mathrm{Re}_\omega = 10^{12}$ are very close, showing that viscosity has a weak influence on the noise intensity for $\mathrm{Re}_\omega > 3200$.

Sound intensities and their derivatives with respect to the Reynolds number

The RMS values of the pressure fluctuations and their derivatives with respect to the Reynolds number obtained using the complex differentiation method for $\mathrm{Re}_\omega = 400$, 800, 1600 and 3200 are shown in Figures 9(a,b,c,d) and 9(e,f,g,h). In all cases, the RMS levels are highest near the middle of the mixing layer, where aerodynamic fluctuations predominate. In the acoustic field for $\mathrm{Re}_\omega = 400$ in Figure 9(a), they are very low, making difficult to visualize the radiation pattern. For $\mathrm{Re}_\omega \geq 800$ in Figures 9(b,c,d), the acoustic intensity is significant within two lobes oriented downstream originating from the position of the vortex pairings. The sound levels increase with the Reynolds number downstream of the pairings, especially in the direction of the lobes for polar angles of $\pm 35°$. As a result, the acoustic radiation becomes more directive as the Reynolds number increases.

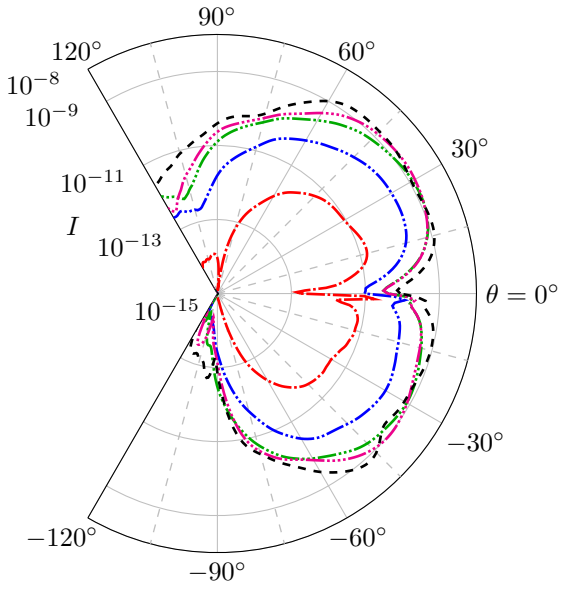

Figure 8: Variations of the acoustic intensity at $r = 200\delta_\omega$ from the vortex pairings as a function of the polar angle θ for —·— $\mathrm{Re}_\omega = 400$, —··— $\mathrm{Re}_\omega = 800$, —···— $\mathrm{Re}_\omega = 1600$, —····— $\mathrm{Re}_\omega = 3200$ and - - - - - $\mathrm{Re}_\omega = 10^{12}$.

For all Reynolds numbers, the derivatives of the RMS values of pressure fluctuations are mostly positive on both sides of the mixing layer, since the noise levels increase with the Reynolds number. For $\mathrm{Re}_\omega = 400$ and $\mathrm{Re}_\omega = 800$ in Figures 9(e,f), the derivatives are positive downstream of the vortex pairings, showing that the sound levels increase with the Reynolds number downstream of the pairings in these cases, in agreement with the sound intensity fields provided for $\mathrm{Re}_\omega \leq 1600$ in Figures 9(a,b,c). For $\mathrm{Re}_\omega = 800$, 1600 and 3200 in Figures 9(f,g,h), the values of the derivatives are highest in two lobes originating from the vortex pairing location and oriented in the main radiation direction, for polar angles of $\pm 35°$, indicating that the acoustic radiation is more directional as the Reynolds number increases. In the shear zone and in the acoustic field, the magnitude of the derivatives decreases with the Reynolds number. This result shows that the effects of the viscosity on the sound radiation are reduced as the Reynolds number increases. For $\mathrm{Re}_\omega = 3200$, the derivatives are negative in two narrow bands oriented downstream and originating slightly further downstream from the position of the vortex pairings, near $x = 200\delta_\omega$. This indicates that a small increase of the Reynolds number leads to a decrease of the sound levels in these two bands for this case.

Acoustic power levels

To quantify the effects of the Reynolds number on the noise levels, the acoustic power levels obtained by integrating the sound intensity determined for the cases with $\mathrm{Re}_\omega \leq 12800$ are plotted in Figure 10 as a function of the Reynolds number. The value estimated for the assumed inviscid case ($\mathrm{Re}_\omega = 10^{12}$) is also provided for comparison. The levels increase strongly from $\mathrm{Re}_\omega = 400$ to $\mathrm{Re}_\omega = 1600$, then weakly from $\mathrm{Re}_\omega = 1600$ to $\mathrm{Re}_\omega = 12800$. The value obtained for $\mathrm{Re}_\omega = 12800$ is very close to the one determined with the assumed inviscid simulation, as expected.

Red segments of arbitrarily chosen lengths with slopes equal to the derivatives of the power levels with respect

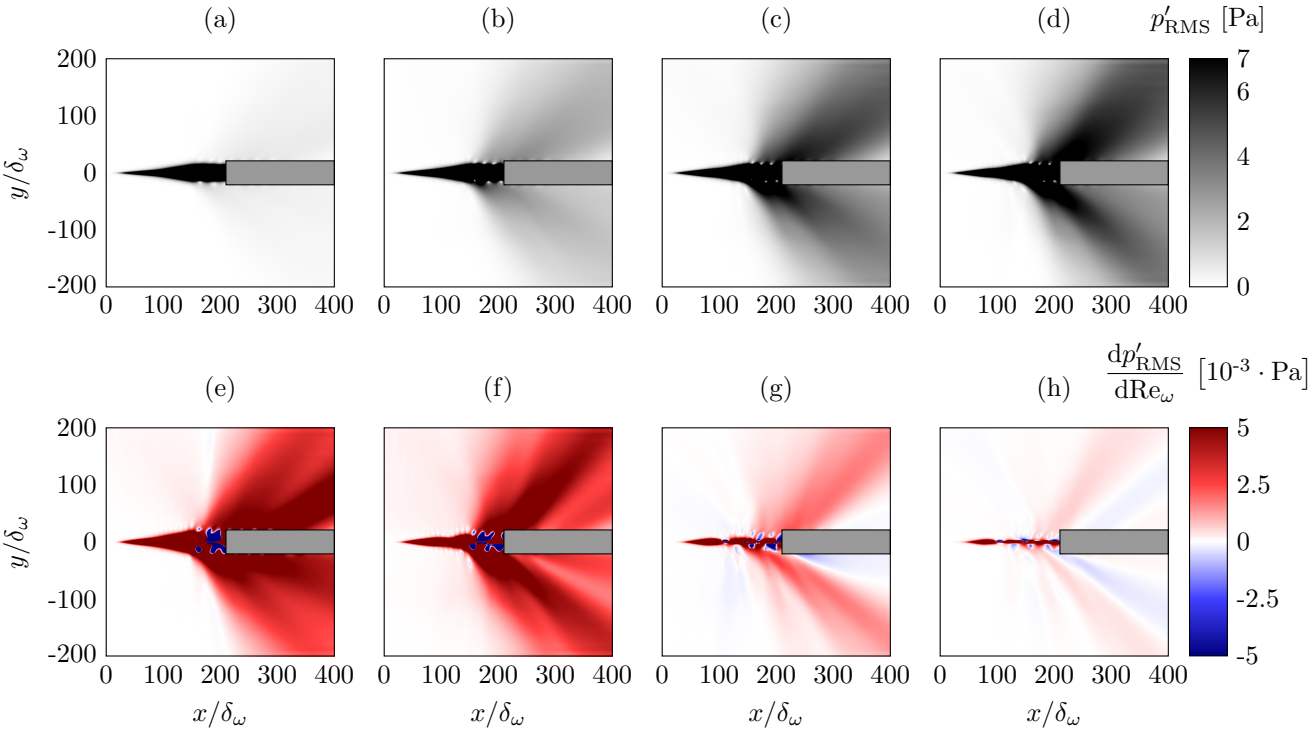

Figure 9: Fields of (a,b,c,d) the RMS values of pressure fluctuations and (d,e,f,g,h) their derivatives with respect to the Reynolds number for (a,e) $\mathrm{Re}_\omega = 400$, (b,f) $\mathrm{Re}_\omega = 800$, (c,g) $\mathrm{Re}_\omega = 1600$ and (d,h) $\mathrm{Re}_\omega = 3200$.

to the Reynolds number are also represented in Figure 10. The slopes are positive since the sound levels increase with the Reynolds number. The values of the derivatives decrease with the Reynolds number, which shows that the sensitivity of the power levels to viscous effects decreases with that flow parameter. The red segments in Figure 10 appear to follow the variations of the sound levels with the Reynolds number. The values of the derivatives of the power levels obtained with the complex differentiation method are thus consistent with the variations of the noise levels values.

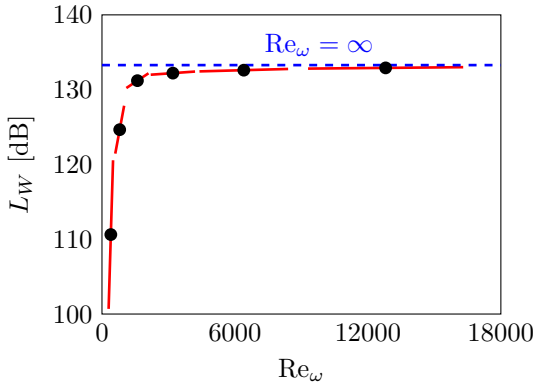

Figure 10: Variations of the acoustic power levels and ——— their derivatives with the Reynolds number; - - - - - power levels for an assumed inviscid flow ($\mathrm{Re}_\omega = 10^{12}$).

6.3. Grid sensitivity

To highlight the effects of the grid resolution on the development of the mixing layer, snapshots of vorticity and of their derivatives with respect to Δy_0, obtained from the simulations of set-Mesh for $\Delta y_0 = 0.1\delta_\omega$, $0.2\delta_\omega$, $0.4\delta_\omega$ and $0.8\delta_\omega$, are displayed in Figures 11(a,c,e,g) and 11(b,d,f,h). For $\Delta y_0 = 0.8\delta_\omega$ in Figure 11(a), the vorticity layer is uniform in the streamwise direction, and do not show any vortices. For $\Delta y_0 = 0.4\delta_\omega$ in Figure 11(c), vortices roll-up near $x = 100\delta_\omega$ and merge near $x = 160\delta_\omega$. In this case, numerical oscillations are seen around the vortices between $x \simeq 100\delta_\omega$ and $x \simeq 200\delta_\omega$. As the mesh spacing decreases from $\Delta y_0 = 0.4\delta_\omega$ to $\Delta y_0 = 0.2\delta_\omega$, the vortex rolling-ups and pairings occur earlier near $x = 75\delta_\omega$ and $x = 150\delta_\omega$, respectively. For $\Delta y_0 = 0.2\delta_\omega$ in Figure 11(e), no numerical oscillations are visible, which suggests that those observed for $\Delta y_0 = 0.4\delta_\omega$ are due to discretization errors. The vorticity fields provided for $\Delta y_0 = 0.2\delta_\omega$ and $\Delta y_0 = 0.1\delta_\omega$ are similar, supporting that the aerodynamic development of the mixing layer is well resolved for $\Delta y_0 \leq 0.2\delta_\omega$.

For $\Delta y_0 = 0.8\delta_\omega$, the derivative of the vorticity in Figure 11(b) is negative at the center of the mixing layer and positive on both sides of the shear zone. This suggests that the vorticity sheet becomes thinner as the mesh spacing Δy_0 decreases in this case, in agreement with the vorticity in Figures 11(a,c) obtained for $\Delta y_0 = 0.4\delta_\omega$ and $\Delta y_0 = 0.8\delta_\omega$. For $\Delta y_0 = 0.8\delta_\omega$, the footprint of the instability waves growing in the shear zone can be seen in the field of the derivatives of the vorticity for $x \geq 175\delta_\omega$. For $\Delta y_0 \leq 0.4\delta_\omega$ in Figures 11(d,f,h), the derivatives have significant values near the vortices. The magnitude of the derivatives become weaker as the mesh spacing Δy_0 decreases. This indicates that the sensitivity of the vortices to the mesh spacing Δy_0 is reduced when the latter decreases, as expected. For $\Delta y_0 = 0.4\delta_\omega$, numerical oscillations similar to the ones observed in the vorticity field obtained for this case are visible. They are more apparent in the derivative field than in the vorticity field. Therefore, the vortices and the numerical oscillations depend on the mesh spacing Δy_0. For $\Delta y_0 = 0.2\delta_\omega$ and $\Delta y_0 = 0.1\delta_\omega$ in Figures 11(f,h), the highest values of the derivatives are found near the vortex rolling-ups and pairings.

Intensity of velocity fluctuations and instability growth rate

The RMS values of the transverse velocity fluctuations obtained at $y = 0$ are plotted in Figure 12(a) using a logarithmic scale. For $\Delta y_0 \leq 0.4\delta_\omega$, the levels first increase strongly, reach a local maximum near the vortex rolling-ups, then decrease slightly, increase thereafter until a maximum is reached in the vicinity of the vortex pairings, and finally do not vary appreciably with the streamwise direction. The RMS values obtained upstream of the vortex rolling-ups decrease with the mesh spacing Δy_0. The levels for $\Delta y_0 = 0.1\delta_\omega$ are however close to those for $\Delta y_0 = 0.2\delta_\omega$. For $\Delta y_0 = 0.8\delta_\omega$, they increase in the streamwise direction while no vortex is observed in this case.

The curves in Figure 12(a) correspond approximately to straight lines between $x = 20\delta_\omega$ and the position of the vortex rolling-ups, indicating that the amplitude of the velocity fluctuations grow exponentially in the streamwise direction. This exponential growth can be characterized by a growth rate $-k_i$, yielding for velocity fluctuations

$$v'(x, y, t) = \hat{v}(y) \cos(k_r x + \omega t) \exp(-k_i x), \tag{44}$$

where $\hat{v}(y)$ is the amplitude, k_r is the wavenumber and ω is the pulsation. The growth rate $-k_i$ is given by the slopes of the straight lines observed in Figure 12(a). It is obtained using a linear fit applied between $x = 20\delta_\omega$

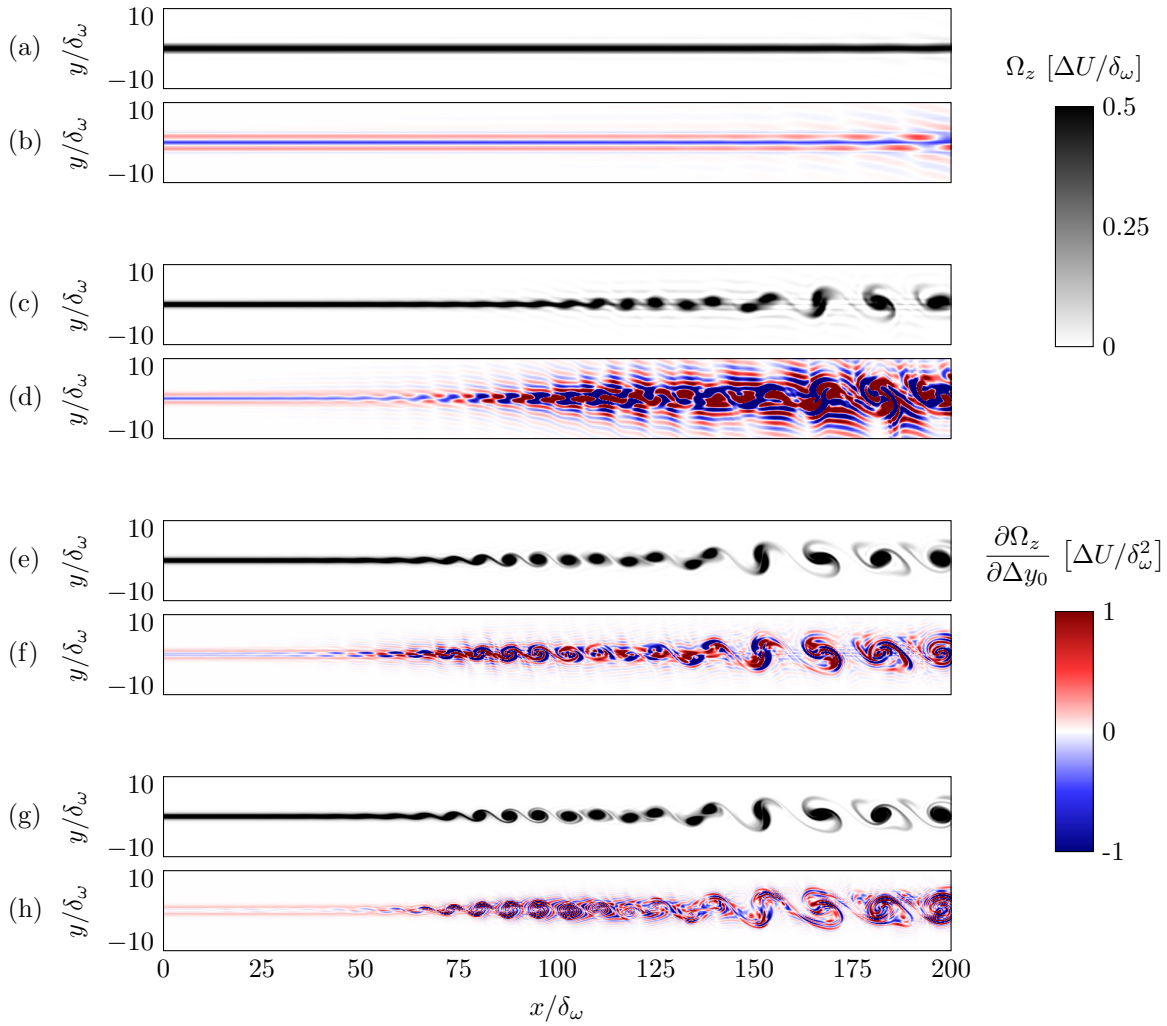

Figure 11: Fields of (a,c,e,g) vorticity Ω_z and (b,d,f,h) their derivatives with respect to Δy_0 for (a,b) $\Delta y_0 = 0.8\delta_\omega$, (c,d) $\Delta y_0 = 0.4\delta_\omega$, (e,f) $\Delta y_0 = 0.2\delta_\omega$ and (g,h) $\Delta y_0 = 0.1\delta_\omega$.

and the position where the RMS levels are equal to one third of their values at the first maximum. The growth rates thus estimated are plotted in Figure 12(b) as a function of the mesh spacing Δy_0. They decrease by 3% from $\Delta y_0 = 0.1\delta_\omega$ to $\Delta y_0 = 0.2\delta_\omega$, then by 24% from $\Delta y_0 = 0.2\delta_\omega$ to $\Delta y_0 = 0.4\delta_\omega$ and finally by 81% from $\Delta y_0 = 0.4\delta_\omega$ to $\Delta y_0 = 0.8\delta_\omega$.

The derivatives of the growth rates with respect to Δy_0 determined using the complex differentiation method are also represented in Figure 12(b). In all cases, the derivatives are negative since the growth rate of the instability waves decreases with the mesh spacing Δy_0. The magnitude of the derivative increases weakly from $\Delta y_0 = 0.1\delta_\omega$ to $\Delta y_0 = 0.2\delta_\omega$, more strongly from $\Delta y_0 = 0.2\delta_\omega$ to $\Delta y_0 = 0.4\delta_\omega$, and weakly from $\Delta y_0 = 0.4\delta_\omega$ to $\Delta y_0 = 0.8\delta_\omega$. They are consistent with the computed growth rates. The value of the derivative of the growth rate for $\Delta y_0 = 0.1\delta_\omega$ is small. This suggests that the growth rate determined for this case is weakly affected by the mesh spacing Δy_0, and thus that it is accurately estimated for $\Delta y_0 = 0.1\delta_\omega$.

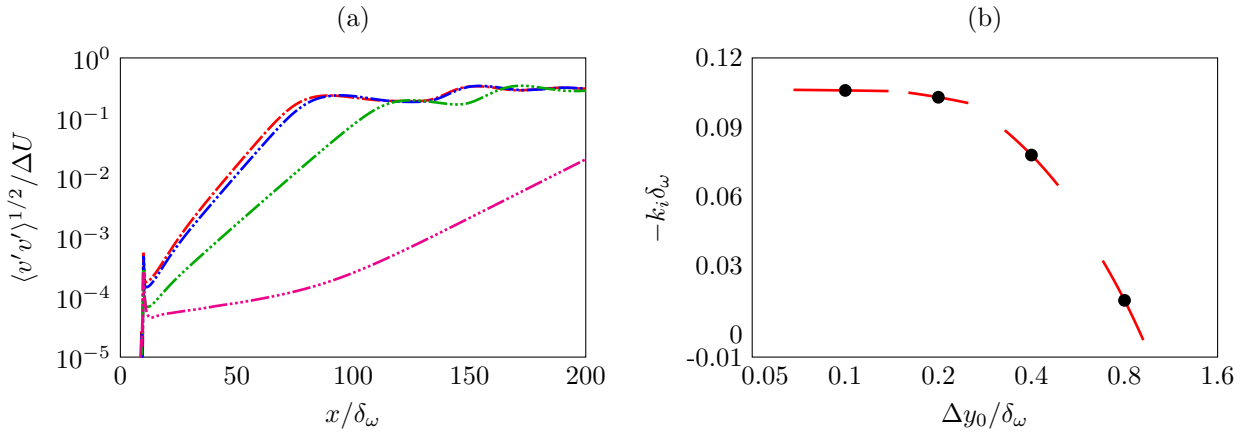

Figure 12: Variations of (a) the RMS values of the transverse velocity fluctuations at the center of the mixing layer for —·— $\Delta y_0 = 0.1\delta_\omega$, —··— $\Delta y_0 = 0.2\delta_\omega$, —···— $\Delta y_0 = 0.4\delta_\omega$ and —····— $\Delta y_0 = 0.8\delta_\omega$ and (b) the growth rate of the instability waves developing initially in the mixing layer and —— the derivatives $\mathrm{d}(-k_i\delta_\omega)/\mathrm{d}\Delta y_0$ as a function of Δy_0. The values of the derivatives are indicated by the red curves.

Pressure fields

Fields of vorticity and fluctuating pressure obtained in the three cases with $\Delta y_0 \leq 0.4\delta_\omega$ for which vortex pairings occur are displayed in Figures 13(a-c). The acoustic pattern is similar to that observed in the case with $\mathrm{M} = 0.3$ and $\mathrm{Re}_\omega = 3200$ provided in Figure 7(d). It does not vary significantly with the mesh spacing Δy_0. For $\Delta y_0 = 0.4\delta_\omega$ and $\Delta y_0 = 0.2\delta_\omega$ in Figures 13(a,b), the amplitude of the pressure fluctuations increases slightly as Δy_0 decreases. The increase in levels is more pronounced in the main radiation direction, for polar angles $\theta \simeq \pm 30°$. The pressure fields for $\Delta y_0 = 0.2\delta_\omega$ and $\Delta y_0 = 0.1\delta_\omega$ are similar, which indicates that the transverse mesh spacing weakly affects the acoustic radiation of the mixing layers for $\Delta y_0 \leq 0.2\delta_\omega$.

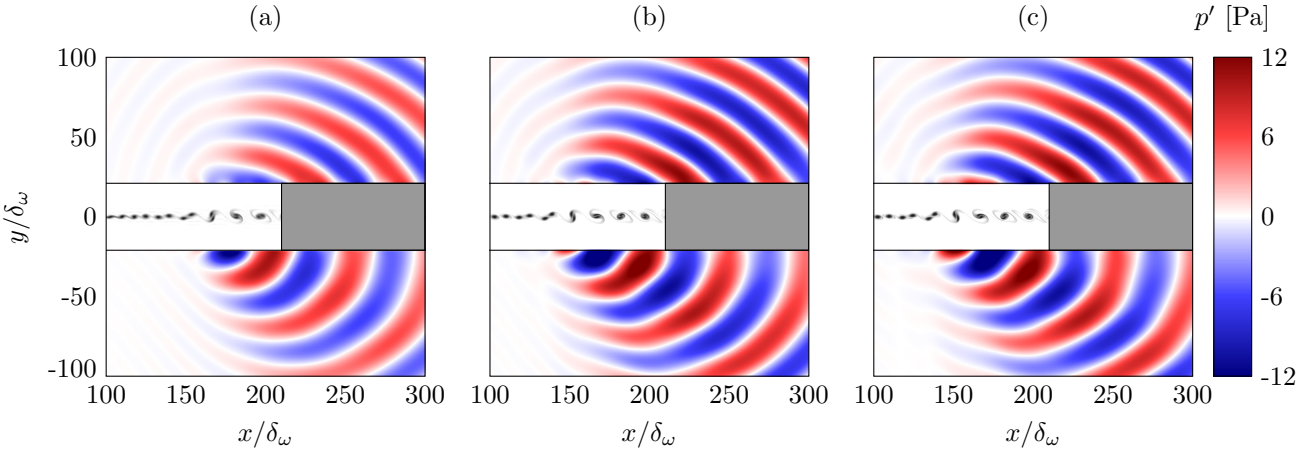

Figure 13: Instantaneous vorticity and fluctuating pressure fields for (a) $\Delta y_0 = 0.4\delta_\omega$, (b) $\Delta y_0 = 0.2\delta_\omega$ and (c) $\Delta y_0 = 0.1\delta_\omega$. The colour scales range from 0 to $\Delta U/\delta_\omega$ for vorticity, from white to black.

Sound directivities

The variations of the sound intensity at $r = 200\delta_\omega$ from the vortex pairings with the polar angle for $\Delta y_0 = 0.1\delta_\omega$, $0.2\delta_\omega$ and $0.4\delta_\omega$ are presented in Figure 14. The noise levels increase as the mesh spacing decreases from $\Delta y_0 = 0.4\delta_\omega$ down to $\Delta y_0 = 0.2\delta_\omega$ and do not vary significantly between $\Delta y_0 = 0.2\delta_\omega$ and $\Delta y_0 = 0.1\delta_\omega$. In the slow flow for $\theta > 0°$, the intensity is maximum for $\theta \simeq 15°$ for $\Delta y_0 = 0.4\delta_\omega$ and for $\theta \simeq 30°$ for $\Delta y_0 \leq 0.2\delta_\omega$. In the fast flow for $\theta < 0°$, it is maximum for $\theta \simeq 30°$ for $\Delta y_0 = 0.4\delta_\omega$ and for $\theta \simeq 37.5°$ for $\Delta y_0 \leq 0.2\delta_\omega$. The acoustic radiation is thus more oriented upstream as the mesh spacing decreases from $\Delta y_0 = 0.4\delta_\omega$ to $\Delta y_0 = 0.2\delta_\omega$.

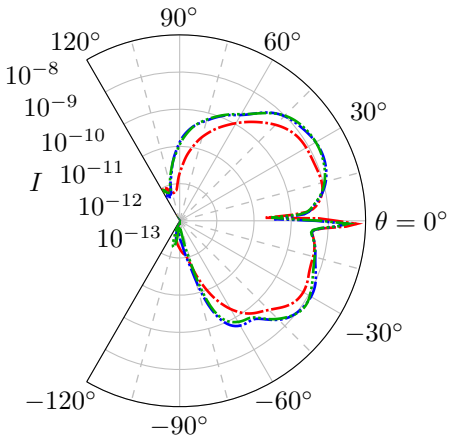

Figure 14: Variations of the acoustic intensity at $r = 200\delta_\omega$ from the vortex pairings as a function of the polar angle θ for —·— $\Delta y_0 = 0.4\delta_\omega$, —··— $\Delta y_0 = 0.2\delta_\omega$ and —···— $\Delta y_0 = 0.1\delta_\omega$.

Sound intensities and their derivatives with respect to the mesh spacing

The RMS values of the pressure fluctuations and their derivatives with respect to Δy_0 obtained with the complex differentiation method for $\Delta y_0 \leq 0.4\delta_\omega$ are represented in Figures 15(a,b,c) and 15(d,e,f), respectively. As the mesh spacing decreases, the sound levels increase from $\Delta y_0 = 0.4\delta_\omega$ to $\Delta y_0 = 0.2\delta_\omega$ and do not seem to vary from $\Delta y_0 = 0.2\delta_\omega$ to $\Delta y_0 = 0.1\delta_\omega$.

For $\Delta y_0 = 0.4\delta_\omega$ in Figure 15(d), the derivatives of the sound intensity are mostly negative in the acoustic field. This indicates that the noise levels decrease with the mesh spacing Δy_0 in this case, in agreement with the acoustic intensities in Figures 15(a,b). In addition, for $\Delta y_0 = 0.4\delta_\omega$, the magnitude of the derivative is higher in the slow flow region for $y > 0$ than in the fast flow region for $y < 0$, suggesting that the sound levels increase more in the first region than is the second one as the mesh spacing Δy_0 decreases in this case. As the mesh spacing decreases from $\Delta y_0 = 0.4\delta_\omega$ to $\Delta y_0 = 0.2\delta_\omega$, the magnitudes of the derivatives become lower, indicating that the sensitivity of the sound levels to Δy_0 is reduced as the grids become finer. For $\Delta y_0 = 0.2\delta_\omega$ and $\Delta y_0 = 0.1\delta_\omega$ in Figures 15(e,f), the derivatives are significant in lobes originating from the vortices between $x \simeq 100\delta_\omega$ and $x \simeq 250\delta_\omega$. In these lobes, they are positive or negative, which suggests that the noise levels increase or decrease at specific positions in the acoustic field as the mesh spacing Δy_0 varies.

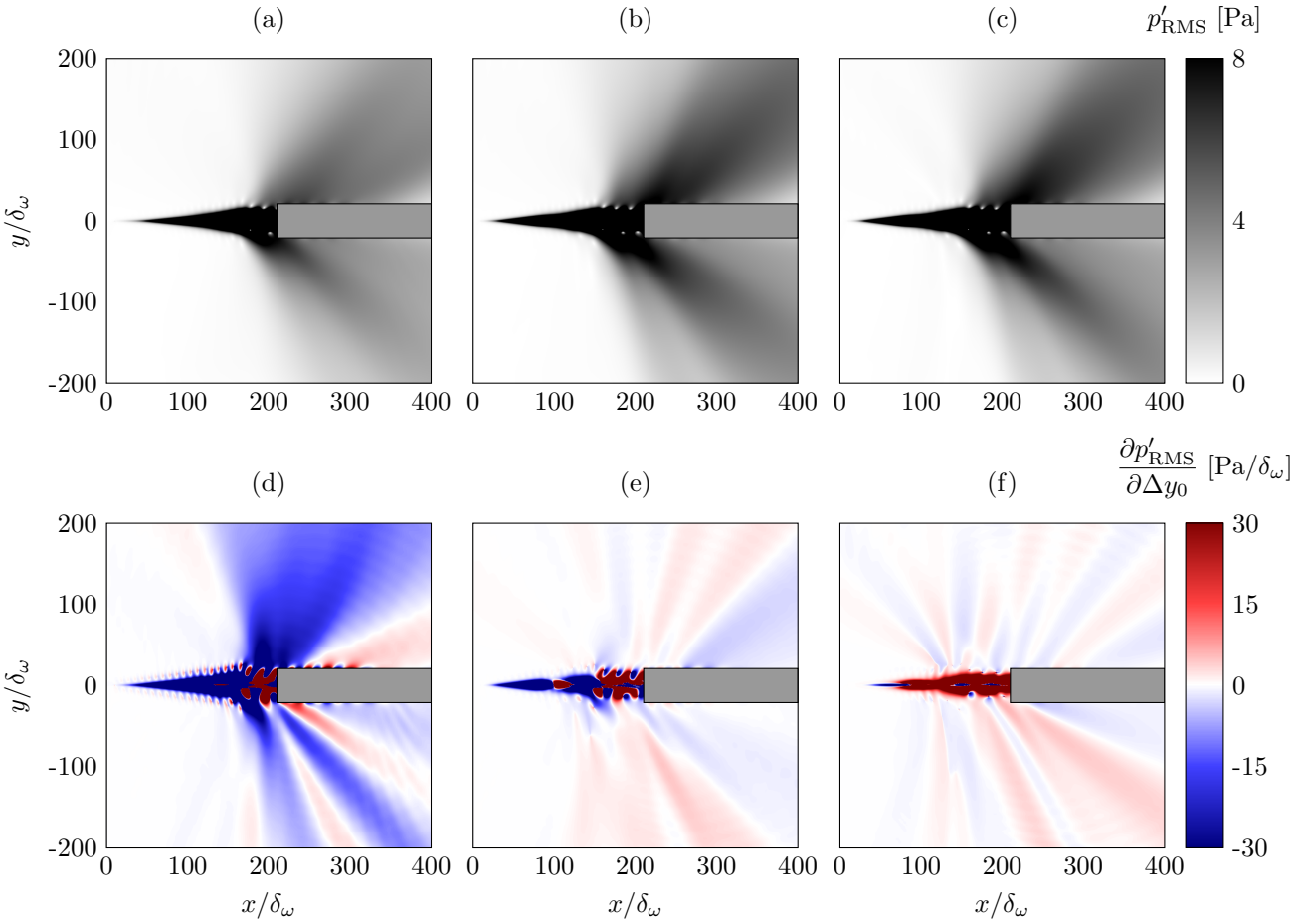

Figure 15: Fields of (a,b,c) the RMS values of pressure fluctuations and (d,e,f) their derivatives with respect to Δy_0 for (a,d) $\Delta y_0 = 0.4\delta_\omega$, (b,e) $\Delta y_0 = 0.2\delta_\omega$ and (c,f) $\Delta y_0 = 0.1\delta_\omega$.

Acoustic power and its sensitivity to the mesh spacing

The acoustic power levels and their derivatives with respect to Δy_0 are represented in Figure 16 as a function of the mesh spacing Δy_0. The sound levels increase by 0.1 dB from $\Delta y_0 = 0.1\delta_\omega$ to $\Delta y_0 = 0.2\delta_\omega$ and decrease by 2.8 dB from $\Delta y_0 = 0.2\delta_\omega$ to $\Delta y_0 = 0.4\delta_\omega$. For $\Delta y_0 = 0.1\delta_\omega$, the derivative is positive, suggesting that the noise levels increase with the mesh spacing in this case. For $\Delta y_0 = 0.2\delta_\omega$ and $\Delta y_0 = 0.4\delta_\omega$, the derivatives are negative, showing that the levels decrease as the mesh spacing increases in these cases. Moreover, the absolute values of the derivatives increase with Δy_0 for $\Delta y_0 \geq 0.2\delta_\omega$. This shows that the sound levels are more affected by the mesh spacing as Δy_0 increases from $\Delta y_0 = 0.2\delta_\omega$ to $\Delta y_0 = 0.4\delta_\omega$ and, therefore, that the sensitivity of the noise levels to the grid resolution is higher when the mesh is coarser. For $\Delta y_0 = 0.1\delta_\omega$ and $\Delta y_0 = 0.2\delta_\omega$, the magnitudes of the derivative are very low compared to the case with $\Delta y_0 = 0.4\delta_\omega$. This indicates that the noise levels are well estimated for $\Delta y_0 \leq 0.2\delta_\omega$.

Quantification of the grid sensitivity

To quantify the sensitivity of the noise levels to the mesh spacing, a grid sensitivity coefficient defined by

$$S_W(h) = L_W(\Delta y_0(1+h)) - L_W(\Delta y_0) \ , \tag{45}$$

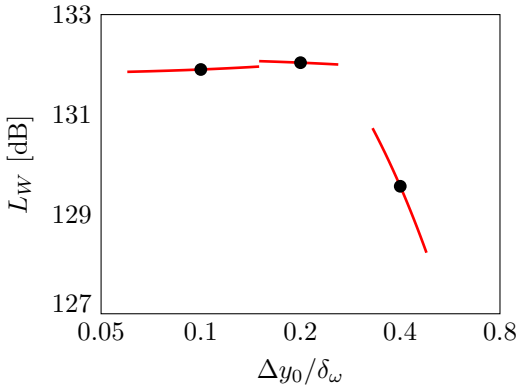

Figure 16: Variations of the sound power levels and ——— their derivatives with the mesh spacing Δy_0.

Table 4: Grid sensitivity coefficient of the sound power levels S_W for $h = 0.1$.

$\Delta y_0/\delta_\omega$	0.1	0.2	0.4
S_W	0.012 dB	−0.012 dB	−0.73 dB

where $h \ll 1$ is a small real number, is considered. In the formula (45), $L_W\left(\Delta y_0\left(1+h\right)\right)$ is the sound power level in dB estimated using a first-order approximation by

$$L_W\left(\Delta y_0\left(1+h\right)\right) \simeq 10\log\left(\frac{W_0 + h\Delta y_0 \dfrac{\partial W_0}{\partial \Delta y_0}}{W_{\text{ref}}}\right), \tag{46}$$

where W_0 is the acoustic power and $\partial W_0/\partial \Delta y_0$ is the derivative of the acoustic power with respect to Δy_0 obtained for a given mesh spacing Δy_0. For instance, for $h = 0.1$, the grid sensitivity coefficient S_W provides a first-order approximation of the gain or loss in dB of the sound power level as the mesh spacing increases by 10%. Therefore, it allows us to quantify the sensitivity of the noise levels to the grid using only the results of a simulation carried out for a given mesh spacing. For example, in the present study, values of S_W have been computed for $\Delta y_0 = 0.1\delta_\omega$, $0.2\delta_\omega$ and $0.4\delta_\omega$ for $h = 0.1$. They are reported in Table 4. For $\Delta y_0 = 0.1\delta_\omega$ and $\Delta y_0 = 0.2\delta_\omega$, S_W is approximately only of 0.1 dB in absolute value. This indicates that the noise levels are almost insensitive to the mesh spacing for $\Delta y_0 \leq 0.2\delta_\omega$. In contrast, for $\Delta y_0 = 0.4\delta_\omega$, the sensitivity coefficient is higher and close to 1 dB in absolute value, showing that the sensitivity of the noise levels to the grid is much stronger in this case.

7. Conclusion

In this paper, the complex differentiation method has been applied to the sensitivity analysis of the noise produced by two-dimensional mixing layers to assess its capabilities to describe the effects of key parameters on the aerodynamic noise. For this purpose, simulations of mixing layers were carried out for Mach numbers between 0.2 and 0.4 and Reynolds numbers between 400 and 12800 on different grids, and the complex differentiation method was applied in each simulation to estimate the derivatives of the sound levels with respect to the parameters under study. Comparisons between derivatives computed using the complex differentiation method and using a first-order

approximation have shown that the first method is more accurate than the second one. The derivatives of the noise levels with respect to the Mach number have highlighted that the acoustic radiation produced by the mixing layer is more intense and less directed downstream as Mach number increases, in good agreement with results obtained using DNS and dimensional analysis. The derivatives of the noise levels with respect to the Reynolds number have indicated that the acoustic radiation is stronger and more pronounced in its main direction as the Reynolds number increases. The complex differentiation method has also been applied to investigate the effects of the transverse mesh spacing at the center of the mixing layer, Δy_0, on the aerodynamic and acoustic fields of a mixing layer by considering grids with $\Delta y_0 = 0.1\delta_\omega$, $0.2\delta_\omega$, $0.4\delta_\omega$ and $0.8\delta_\omega$. The derivatives of the sound levels with respect to the mesh parameter have shown that the noise levels decrease with the mesh spacing Δy_0, in agreement with results from parametric studies. The results provided in this paper thus suggest that the complex differentiation method can be applied using DNS to investigate the sensitivity of the noise produced by a flow to physical parameters, and to perform grid sensitivity analyses of this noise. In future studies, it may be interesting to use the complex differentiation method to study the grid sensitivity of three-dimensional turbulent flows computed using large-eddy simulations.

Acknowledgments

The first author was supported by the FUI25 CALM-AA (CiblAge des sources par voie Logicielle et Méthodes inverses pour l'AéroAcoustique) regional project, co-financed by the European regional development fund. This work was granted access to the HPC resources of PMCS2I (Pôle de Modélisation et de Calcul en Sciences de l'Ingénieur de l'Information) of Ecole Centrale de Lyon. It was performed within the framework of the LABEX CeLyA (ANR-10-LABX-0060) of Université de Lyon, within the program Investissements d'Avenir (ANR-16-IDEX-0005) operated by the French National Research Agency (ANR). For the purpose of Open Access, a CC-BY public copyright licence has been applied by the authors to the present document and will be applied to all subsequent versions up to the Author Accepted Manuscript arising from this submission.

Financial disclosure

None reported.

Conflict of interest

The authors declare no potential conflict of interests.

References

[1] J. R. R. A. Martins, J. T. Hwang, Review and unification of methods for computing derivatives of multidisciplinary computational models, AIAA J. 51 (2013) 2582–2599. doi:10.2514/1.J052184.

[2] R. D. Kirkman, M. Metzger, Sensitivity analysis of low Reynolds number channel flow using the finite volume method, Int. J. Numer. Methods Fluids 57 (2008) 1023–1045. doi:https://doi.org/10.1002/fld.1669.

[3] C. Fiorini, B. Després, M. A. Puscas, Sensitivity equation method for the Navier-Stokes equations applied to uncertainty propagation, Int. J. Numer. Methods Fluids 93 (2021) 71–92. doi:https://doi.org/10.1002/fld.4875.

[4] J. Borggaard, J. Burns, A PDE sensitivity equation method for optimal aerodynamic design, J. Comput. Phys. 136 (1997) 366–384. doi:https://doi.org/10.1006/jcph.1997.5743.

[5] H. Hristova, S. Étienne, D. Pelletier, J. Borggaard, A continuous sensitivity equation method for time-dependent incompressible laminar flows, Int. J. Numer. Methods Fluids 50 (2006) 817–844. doi:https://doi.org/10.1002/fld.1079.

[6] M. Zayernouri, M. Metzger, Coherent features in the sensitivity field of a planar mixing layer, Phys. Fluids 23 (2011) 025105. doi:10.1063/1.3546174.

[7] J. N. Lyness, C. B. Moler, Numerical differentiation of analytic functions, SIAM J. Numer. Anal. 4 (1967) 202–210. doi:10.1137/0704019.

[8] W. K. Anderson, J. C. Newman, D. L. Whitfield, E. J. Nielsen, Sensitivity analysis for Navier-Stokes equations on unstructured meshes using complex variables, AIAA J. 39 (2001) 56–63. doi:10.2514/2.1270.

[9] S.-Y. Lu, P. Sagaut, Direct sensitivity analysis for smooth unsteady compressible flows using complex differentiation, Int. J. Numer. Methods Fluids 53 (2007) 1863–1886. doi:https://doi.org/10.1002/fld.1386.

[10] J. R. R. A. Martins, P. Sturdza, J. J. Alonso, The complex-step derivative approximation, ACM Trans. Math. Softw. 29 (2003) 245–262. doi:10.1145/838250.838251.

[11] R. D. Kirkman, M. Metzger, Direct numerical simulation of sensitivity coefficients in low Reynolds number turbulent channel flow, J. Turbul. 10 (2009) N23. doi:10.1080/14685240902960173.

[12] W. Squire, G. Trapp, Using complex variables to estimate derivatives of real functions, SIAM Review 40 (1998) 110–112. doi:10.1137/S003614459631241X.

[13] V. Vatsa, Computation of sensitivity derivatives of Navier–Stokes equations using complex variables, Adv. Eng. Softw. 31 (2000) 655–659. doi:https://doi.org/10.1016/S0965-9978(00)00025-9.

[14] L. Cerviño, T. Bewley, J. Freund, S. Lele, Perturbation and adjoint analyses of flow-acoustic interactions in an unsteady 2D jet, CTR Proc. Summ. Prog (2002) 27–39.

[15] E. Vergnault, P. Sagaut, Application of lattice Boltzmann method to sensitivity analysis via complex differentiation, J. Comput. Phys. 230 (2011) 5417–5429. doi:https://doi.org/10.1016/j.jcp.2011.03.044.

[16] A. Deneuve, P. Druault, R. Marchiano, P. Sagaut, A coupled time-reversal/complex differentiation method for aeroacoustic sensitivity analysis: towards a source detection procedure, J. Fluid Mech. 642 (2010) 181–212. doi:10.1017/S0022112009991704.

[17] P. J. Roache, Verification and validation in computational science and engineering, volume 895, Hermosa Albuquerque, NM, 1998.

[18] T. Colonius, S. Lele, P. Moin, Sound generation in a mixing layer, J. Fluid Mech. 330 (1997). doi:10.1017/S0022112096003928.

[19] C. Bogey, C. Bailly, D. Juve, Numerical simulation of sound generated by vortex pairing in a mixing layer, AIAA J. 38 (2000) 2210–2218. doi:10.2514/2.906.

[20] C. Moser, E. Lamballais, F. Margnat, V. Fortuné, Y. Gervais, Numerical study of Mach number and thermal effects on sound radiation by a mixing layer, Int. J. Aeroacoust. 11 (2012) 555–579. doi:10.1260/1475-472X.11.5-6.555.

[21] P. A. Monkewitz, P. Huerre, Influence of the velocity ratio on the spatial instability of mixing layers, Phys. Fluids 25 (1982) 1137–1143. doi:10.1063/1.863880.

[22] C. Bogey, C. Bailly, A family of low dispersive and low dissipative explicit schemes for flow and noise computations, J. Comput. Phys. 194 (2004) 194–214. doi:https://doi.org/10.1016/j.jcp.2003.09.003.

[23] C. Bogey, N. de Cacqueray, C. Bailly, A shock-capturing methodology based on adaptative spatial filtering for high-order non-linear computations, J. Comput. Phys. 228 (2009) 1447–1465. doi:https://doi.org/10.1016/j.jcp.2008.10.042.

[24] J. Berland, C. Bogey, O. Marsden, C. Bailly, High-order, low dispersive and low dissipative explicit schemes for multiple-scale and boundary problems, J. Comput. Phys. 224 (2007) 637–662. doi:https://doi.org/10.1016/j.jcp.2006.10.017.

[25] C. K. Tam, Z. Dong, Radiation and outflow boundary conditions for direct computation of acoustic and flow disturbances in a nonuniform mean flow, J. Comput. Acoust. 04 (1996) 175–201. doi:10.1142/S0218396X96000040.

[26] J. Martins, P. Sturdza, J. Alonso, The connection between the complex-step derivative approximation and algorithmic differentiation, in: AIAA Paper, 2001, p. 921. doi:10.2514/6.2001-921.

[27] J. E. Ffowcs Williams, Hydrodynamic noise, Annu. Rev. Fluid Mech. 1 (1969) 197–222. doi:10.1146/annurev.fl.01.010169.001213.

[28] Y. P. Guo, Application of the Ffowcs Williams/Hawkings equation to two-dimensional problems, J. Fluid Mech. 403 (2000) 201–221. doi:10.1017/S0022112099006989.

[29] M. J. Lighthill, On sound generated aerodynamically I. general theory, Proc. R. Soc. Lond. Ser. A 211 (1952) 564–587. doi:10.1098/rspa.1952.0060.

[30] H. S. Ribner, Quadrupole correlations governing the pattern of jet noise, J. Fluid Mech. 38 (1969) 1–24. doi:10.1017/S0022112069000012.

[31] J. B. Freund, Noise-source turbulence statistics and the noise from a Mach 0.9 jet, Phys. Fluids 15 (2003) 1788–1799. doi:10.1063/1.1569919.